Early Holocene and Late Pleistocene slip rates of the southern Dead Sea Fault determined from 10Be cosmogenic dating of offset alluvial deposits

Maryline Le Béon, Yann Klinger, Mahmoud Al-Qaryouti, Anne-Sophie Mériaux, Robert C. Finkel, Ata Elias, Omar Mayyas, Frederick J. Ryerson, Paul Tapponnier

To cite this version:

Maryline Le Béon, Yann Klinger, Mahmoud Al-Qaryouti, Anne-Sophie Mériaux, Robert C. Finkel, et al.. Early Holocene and Late Pleistocene slip rates of the southern Dead Sea Fault determined from 10Be cosmogenic dating of offset alluvial deposits. Journal of Geophysical Research : Solid Earth, 2010, 115, ⟨10.1029/2009JB007198⟩. ⟨insu-03605277⟩

HAL Id: insu-03605277
https://insu.hal.science/insu-03605277v1

Submitted on 11 Mar 2022

JOURNAL OF GEOPHYSICAL RESEARCH, VOL. 115, B11414, doi:10.1029/2009JB007198, 2010

Early Holocene and Late Pleistocene slip rates of the southern Dead Sea Fault determined from ^{10}Be cosmogenic dating of offset alluvial deposits

Maryline Le Béon,[1,2] Yann Klinger,[1] Mahmoud Al-Qaryouti,[3] Anne-Sophie Mériaux,[4]
Robert C. Finkel,[5,6] Ata Elias,[7] Omar Mayyas,[3] Frederick J. Ryerson,[8]
and Paul Tapponnier[1,9]

Received 9 December 2009; revised 27 May 2010; accepted 13 July 2010; published 25 November 2010.

[1] Two sites located along the Wadi Araba Fault (WAF) segment of the Dead Sea Fault are targeted for tectonic-morphological analysis. ^{10}Be cosmogenic radionuclide (CRN) dating of embedded cobbles is used to constrain the age of offset alluvial surfaces. At the first site a 48 ± 7 m offset alluvial fan, for which ^{10}Be CRN model ages average 11.1 ± 4.3 ka, yield a slip rate of 5.4 ± 2.7 mm/a, with conservative bounds of 1.3–16.4 mm/a. At the second site the scattered distributions of the ^{10}Be CRN ages from an offset bajada attest to the complex processes involved in sediment transport and emplacement. There, two offsets were identified. The 160 ± 8 m offset of an incised alluvial fan dated at 37 ± 5 ka shows a slip rate of 4.5 ± 0.9 mm/a, with a conservative minimum value of 3.2 mm/a. A larger offset, 626 ± 37 m, is derived from a prominent channel incised into the bajada. Cobbles from the bajada surface have ages from 33 to 141 ka, with a mean of 87 ± 26 ka. A slip rate of 8.1 ± 2.9 mm/a is derived from the mean age, with conservative bounds of 3.8–22.1 mm/a. These results and other published slip rates along the linear WAF segment, from GPS to geological time scales, lack the resolution to fully resolve the question of temporal variations versus consistency of the fault slip rate of the WAF. Yet, given the uncertainties, they are not inconsistent with each other.

Citation: Le Béon, M., Y. Klinger, M. Al-Qaryouti, A.-S. Mériaux, R. C. Finkel, A. Elias, O. Mayyas, F. J. Ryerson, and P. Tapponnier (2010), Early Holocene and Late Pleistocene slip rates of the southern Dead Sea Fault determined from ^{10}Be cosmogenic dating of offset alluvial deposits, *J. Geophys. Res.*, *115*, B11414, doi:10.1029/2009JB007198.

1. Introduction

[2] Branching off the northern tip of the Red Sea spreading center, the Dead Sea Fault (DSF) is a 1000 km long left-lateral strike-slip fault, allowing northward motion of Arabia relative to Africa and Sinai (Figure 1a). To the north the DSF links up with the East Anatolian Fault system at the collision zone between Arabia and Eurasia. Present-day and long-term slip rates of the southern DSF, south of Lebanon, seem to be fairly well agreed on. Recent GPS profiles across the fault and regional GPS data both point to a slip rate of 4–6 mm/a for the last ~10 years [e.g., *Reilinger et al.*, 2006; *Le Béon et al.*, 2008]. Geological Miocene formations are offset 40 to 45 km and yield a slip rate of 3.3–6.4 mm/a [*Quennell*, 1958, 1959; *Freund et al.*, 1968, 1970]. Finally, closing the 30 km pull-apart basins of the Dead Sea and the Gulf of Aqaba, which formed during the Early Pliocene, yields a slip rate of 6 mm/a [*Garfunkel*, 1981; *Garfunkel and Ben-Avraham*, 2001]. By contrast, Holocene and Late Pleistocene slip rates are still subject to large uncertainties, with values ranging from 2 to 10 mm/a [*Galli*, 1999; *Klinger et al.*, 2000a; *Niemi et al.*, 2001; *Marco et al.*, 2005; *Ferry et al.*, 2007].

[3] This study provides new constraints on the Early Holocene and Late Pleistocene slip rates on the DSF, focusing on the Wadi Araba Fault (WAF) segment (Figure 1b). The WAF strikes N12°E for about 160 km, from the cities of Aqaba and Elat to the Dead Sea. The trace of the active fault is well expressed in the Quaternary morphology, owing to arid climatic conditions. Hence, numerous offset geomorphic features such as channels and alluvial surfaces can be observed, as well as small push-up and pull-apart structures.

[4] In this study, we targeted two sites, about 100 km apart (Figure 1b), where the WAF displaced numerous

---

[1] Equipe de Tectonique, Institut de Physique du Globe de Paris, Paris, France.

[2] Now at Department of Geosciences, National Taiwan University, Taipei, Taiwan.

[3] Seismology Division, Natural Resources Authority, Amman, Jordan.

[4] School of Geography, Politics and Sociology, Newcastle University, Newcastle upon Tyne, UK.

[5] EPS Department, University of California Berkeley, Berkeley, California, USA.

[6] Now at Centre Europeen de Recherche et d'Enseignement des Geosciences de l'Environnement, Europole Mediterraneen de l'Arbois, Aix-en-Provence, France.

[7] Geology Department, American University of Beirut, Beirut, Lebanon.

[8] Institute of Geophysics and Planetary Physics, Lawrence Livermore National Laboratory, Livermore, California, USA.

[9] Now at Earth Observatory of Singapore, Nanyang Technological University, Singapore.

0148-0227/10/2009JB007198

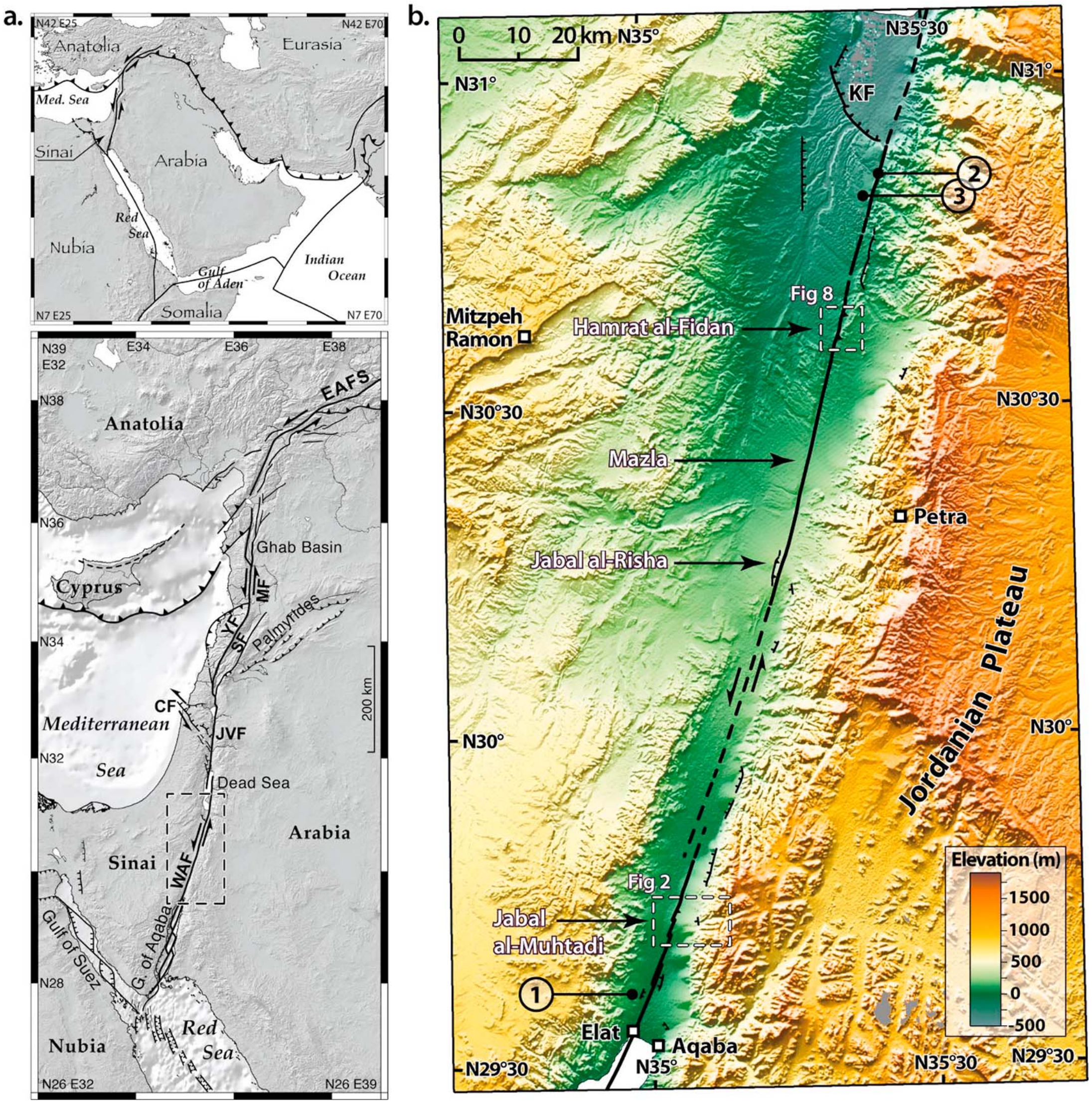

Figure 1. (a) Regional tectonic setting of this study. Tectonic map is modified from *Daëron et al.* [2004] and *Elias et al.* [2007]. WAF, Wadi Araba Fault; JVF, Jordan Valley Fault; CF, Carmel Fault; YF, Yammouneh Fault; SF, Serghaya Fault; MF, Missyaf Fault; EAFS, East Anatolian Fault system. Box shows location of Figure 1b. (b) Active faults in the Wadi Araba and location of the study sites over SRTM3 (pixel size, ~90 m) topography. KF, Khunayzir Fault. Circled numbers show locations of the study sites of (1) *Porat et al.* [2010], (2) *Niemi et al.* [2001] and *Klinger et al.* [2000a] (Early Holocene), and (3) *Klinger et al.* [2000a] (Late Pleistocene).

alluvial surfaces. First, we describe morphological evidence for left-lateral offsets of alluvial surfaces and channels at each site. Next, on the basis of ^{10}Be cosmogenic radionuclide (CRN) model ages to constrain the ages of the surfaces, we derive fault slip rates. Finally, we compare our results with previous results obtained on the WAF segment for various time scales to discuss fault behavior and the possible distribution of earthquakes through time.

2. Geomorphic Analysis

2.1. The Jabal Al-Muhtadi Site

2.1.1. Setting and Geomorphic Mapping

[5] The Jabal al-Muhtadi site is located in the southern Wadi Araba (Figure 1b). There, the WAF, clearly visible, cuts through the distal part of an alluvial fan deposited at the mouth of the Wadi al-Muhtadi (Figure 2). The fan slopes ~3.5° westward for ~4.5 km, from the foot of the Jordanian Plateau to the center of the valley. The alluvial deposits are mostly composed of granitic clasts originating from the Precambrian bedrock [*Rashdan*, 1987] drained by Wadi al-Muhtadi.

[6] At the southern tip of the fan, steps in the fault trace to the west produce two small pull-apart basins filled by recent sediments that appear in a light gray color on the SPOT5 image (pixel size, ~2.8 m). Farther north, a change in fault azimuth from N18°E to N24°E locally induces a reverse component of slip responsible for the uplift and subsequent incision of alluvial deposits [e.g., *Meyer et al.*, 1998]

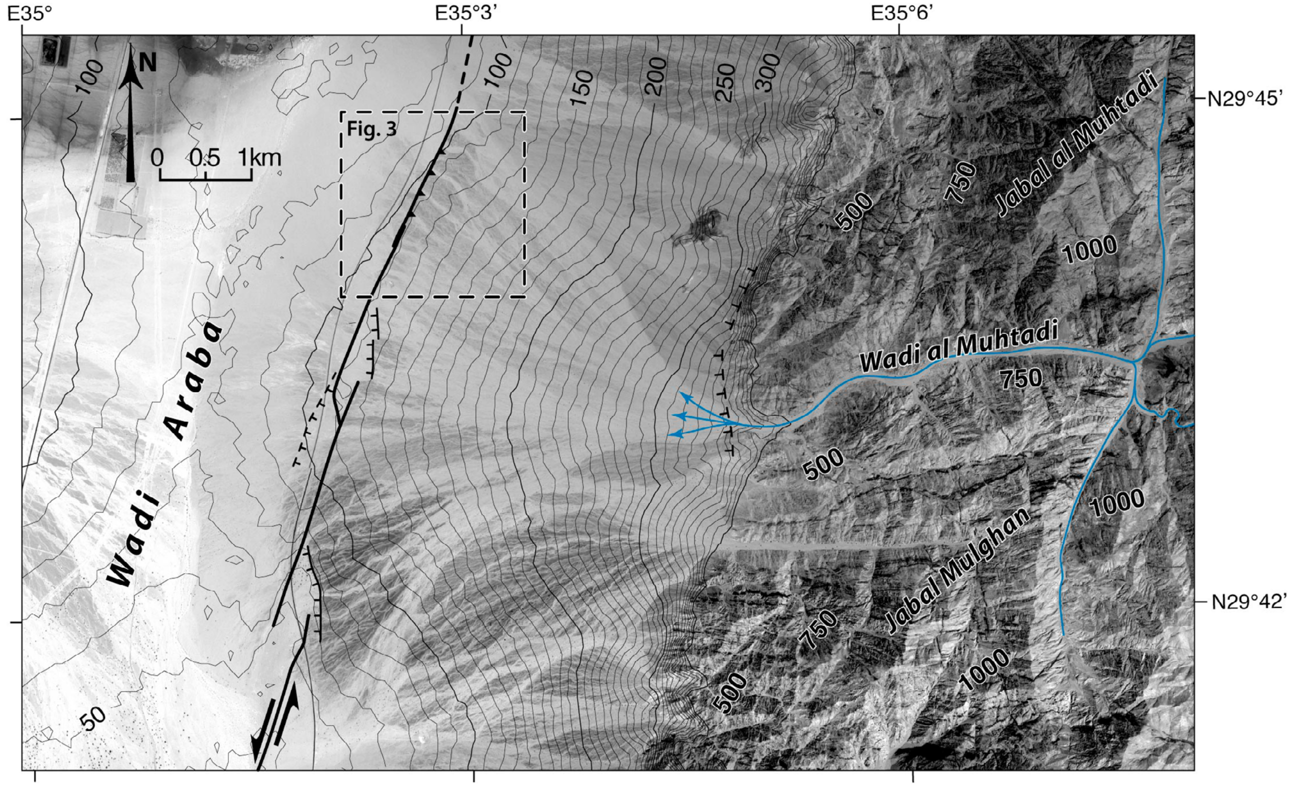

Figure 2. Overview of the Wadi Al-Muhtadi alluvial fan. Topographic contour lines (SRTM3) are displayed over the SPOT5 image. Blue lines underline the Wadi Al-Muhtadi drainage network.

(Figures 2 and 3). Several offsets of rills and of recent alluvial deposits can clearly be observed at this site.

[7] Three distinct levels of alluvial surfaces can be identified from morphologic criteria. Relative ages are determined as a function of surface height above the present-day stream beds, degree of incision by surficial rills, and surface darkness related to the development of desert varnish and desert pavement, typical in arid areas [*Bull*, 1991; *Quade*, 2001]. Observations have been collected in the field and from analysis of satellite imagery, high-resolution Google Earth imagery database, aerial photographs (pixel size, ~0.4 m), and 1/50,000 topographic maps. At this site the three levels of alluvial surfaces above the active channels are labeled F1 to F3, with F3 being the oldest (Figure 3).

[8] Upstream from the fault trace, uplift and later incision of alluvial surfaces allowed preservation of the upper level, F3 (Figure 3). Standing ~5 m above the active stream beds and smooth in appearance on satellite views, F3 is easy to identify and has a surface pavement composed of coarse pebbles. Downstream from the fault, only a few remains of F3 are observed, as most of F3 has been laterally eroded by the active channels (Figure 4a).

[9] Downstream from the fault trace the lower surfaces, F1, stand about 40 cm above the active stream beds and are characterized by a very light surface color and shallow incision by surficial rills, which point toward the mouth of the drainages incised into F3 (Figure 3). East of the fault, surfaces F1 can be traced upstream for several meters within the channels. Hence F1 is inset into F3, with fans developing at the outlet of the channels incised into F3.

[10] Downstream from the fault trace the intermediate level F2 is limited to a few patches, mostly south of the mouth of channels C2 and C3 (Figure 3). They are sheltered from the water flow, lying just below uplifted surfaces F3, located on the eastern block. These darker flat surfaces on satellite imagery stand about 40 cm above F1 (Figure 4b). Similarly to F1, incision by surficial rills also shows a SW-to-WSW-radiating pattern pointing to the former location of feeding channels, before they got offset owing to slip on the fault. Upstream from the fault a small dark surface of a similar relative height above F1 has also been identified within channel C3 (Figures 3 and 4b). Upstream from the perched surfaces F3, we observed surfaces that are lighter than F3, less incised, and of a lower height above the active channels, which may correlate with surfaces F2.

2.1.2. Offset Measurements

[11] The disparity in alluvial surface preservation east and west of the fault illustrates the lateral erosion of terrace material by the active channels related to incision and lateral displacements along the WAF. Although all the alluvial fans are cut and displaced by the active fault, the clearest offset is determined from the best-preserved fan F2, located at the outlet of channel C3 (Figures 3–5). On the fan surface F2, downstream from the fault, the radial pattern of incision by surficial rills enables us to estimate the position of the apex of the fan (Figure 5b). Moreover, the incision pattern and the geometry of the southern extent of the fan, concave toward the apex, show that the southern edge of F2 has been preserved. By contrast, the missing WNW-to-NW-oriented surficial rills and the fairly straight northern edge of the fan

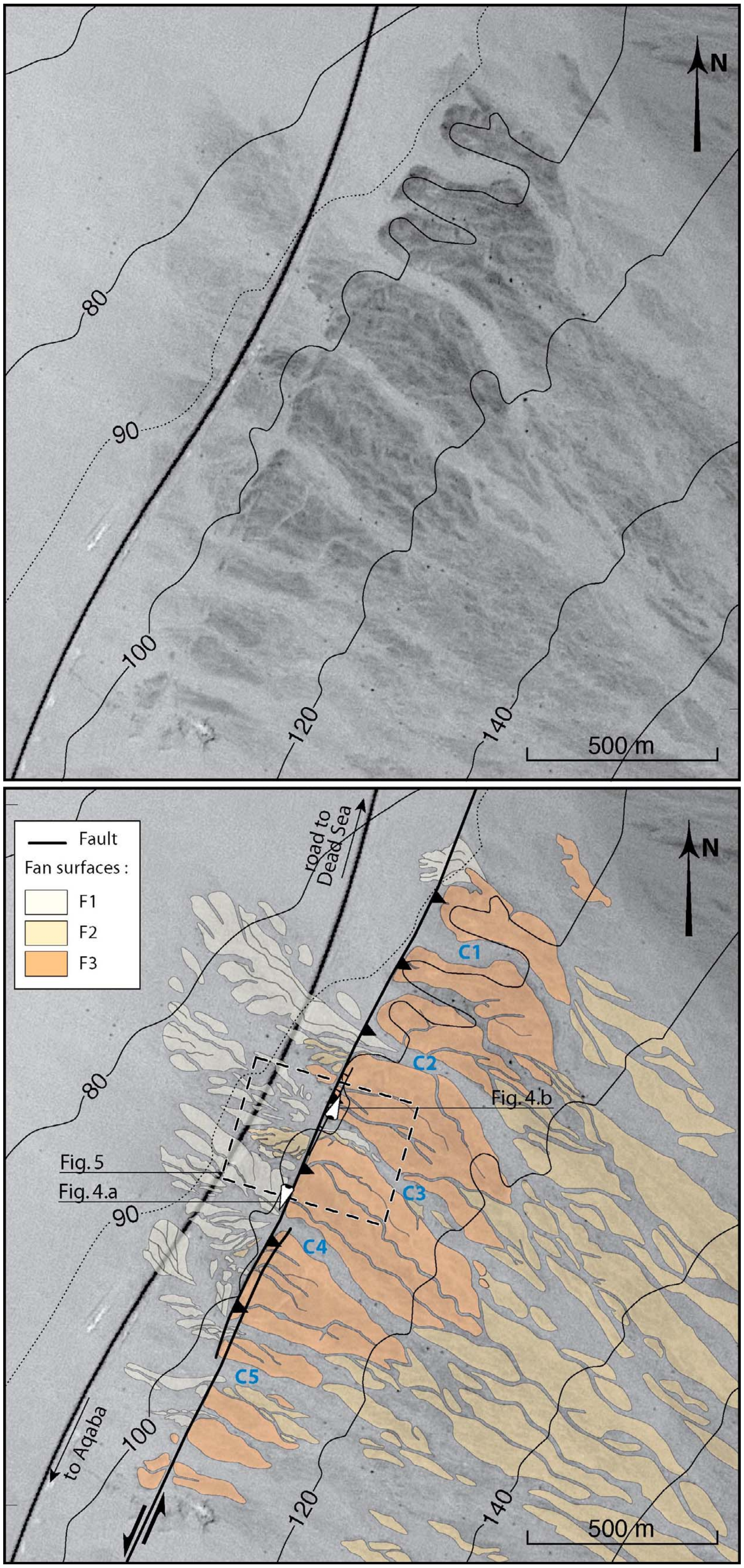

Figure 3. Morphotectonic map of the Jabal Al-Muhtadi site over the SPOT5 image. Relative age of alluvial surfaces increases from F1 to F3. Topographic contour lines are digitalized from 1/50,000 topographic maps.

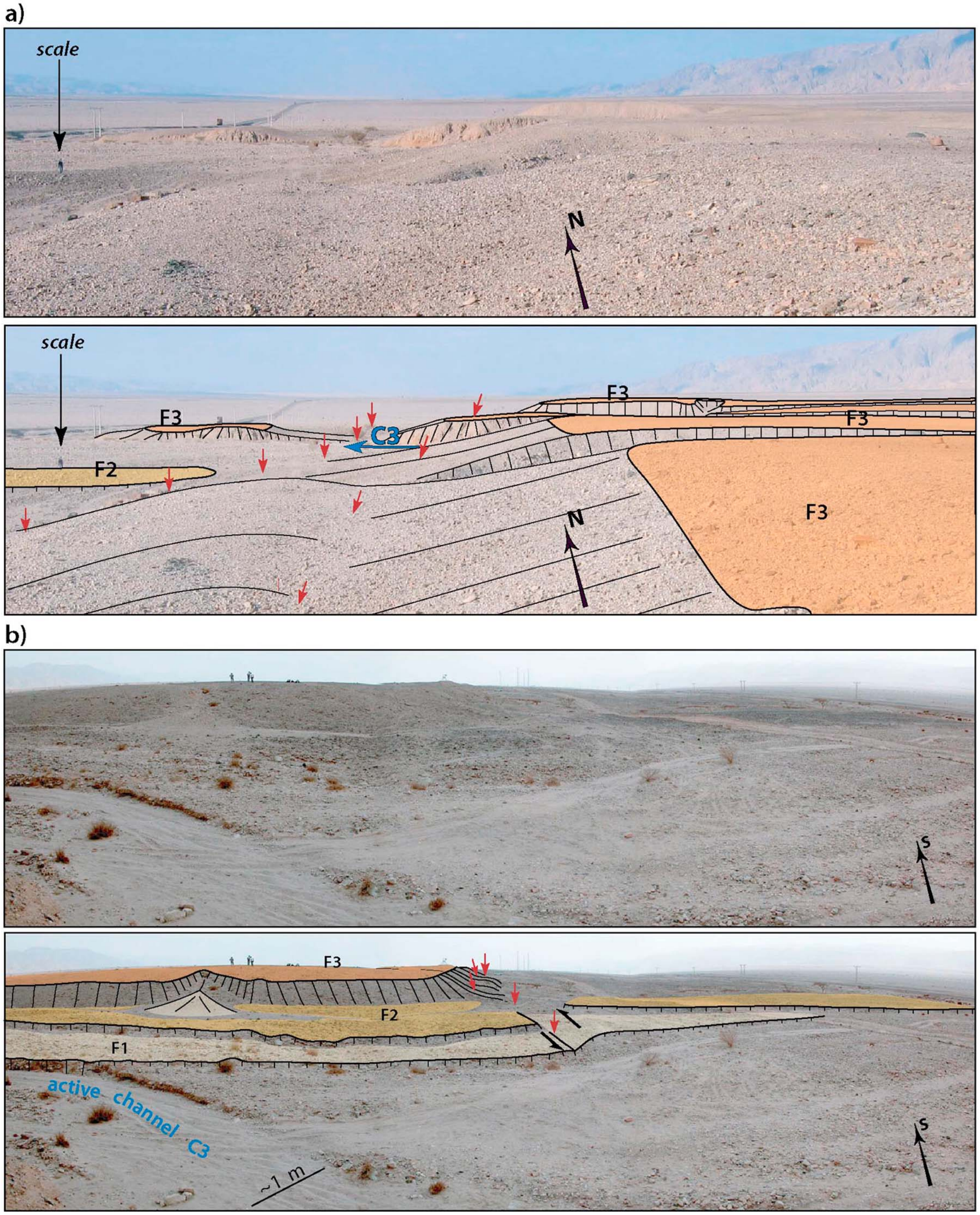

Figure 4. Field views and geomorphic interpretations of the Jabal Al-Muhtadi site. Red arrows point to the fault trace. (a) View of the height of the F3 surfaces relative to the younger fans and present-day streams. For scale, there is a man at the left in the photograph, standing on F2. (b) Sequence of alluvial surfaces from F3 to F1.

attest to an erosive relationship between F2 and F1. From what remains of the incision pattern, about half of the fan would have been eroded away during the emplacement of F1 in channel C3. Assuming an initial symmetrical shape, we could estimate the possible extent of the original fan surface to the north. The accuracy, however, is limited by the asymmetric geometry of the rims of C3, which are wide-mouthed to the south and straight to the north.

[12] We determine the offset of the alluvial surface F2 by restoring the western fan surface F2 to its initial location, in front of the mouth of C3. It is unlikely that the fan surface F2 downstream originates in C1 or C2, as F2 should have

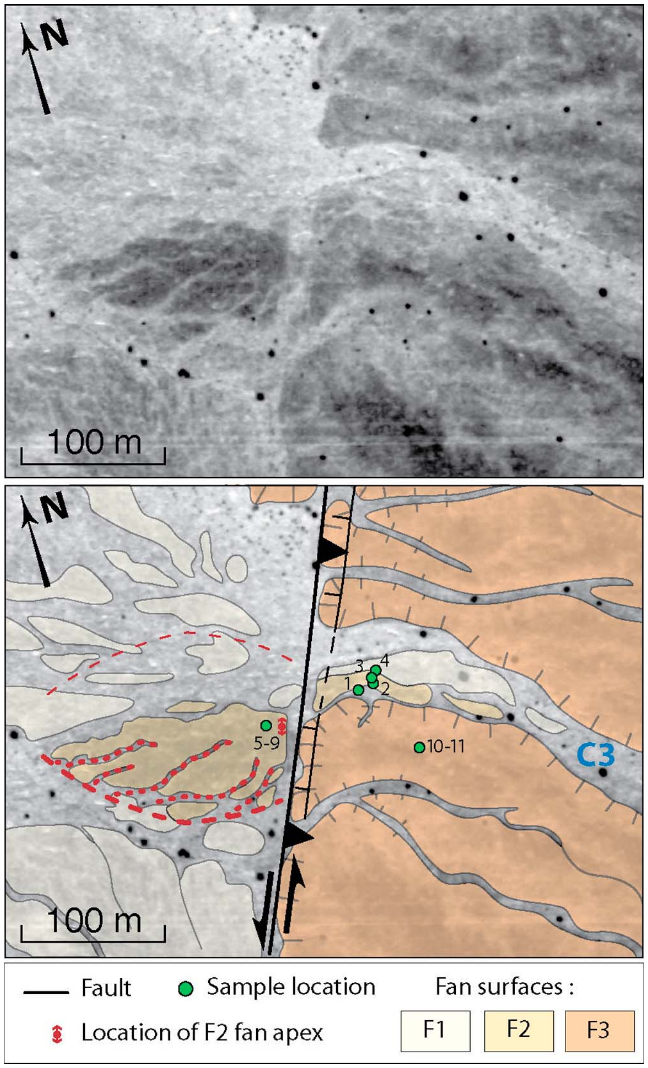

Figure 5. Aerial photograph and morphotectonic map of the offset alluvial surface F2 located south of the mouth of channel C3, at the Jabal Al-Muhtadi site. In the lower box, red circles represent surficial rills incised in fan F2 used to estimate the fan apex position, shown by the red circle with red arrowheads above and below, indicating the position uncertainty. Dashed red lines represent the extent of fan F2 (see text).

been dismantled when passing in front of other active channels. The southern edge of the fan surface F2, in particular, would have been especially vulnerable.

[13] Hereafter, we describe successively the most reasonable reconstruction, minimum possible offset, and maximum possible offset at this site (Figure 6). The most likely reconstruction is obtained by realigning the apex of the downstream fan with the upstream channel axis and the southern edges of F2, ensuring continuity between the riser F2/F3 upstream and the riser F1/F2 downstream (Figure 6a). In this reconstruction the location of the inferred northern edge of the fan would also be consistent with the position of the northern bank of C3. We obtain an offset of 48 ± 7 m. Lower and upper bounds are arguably based on acceptable curvature of the southernmost water flow that emplaced F2. However, larger or smaller offsets would imply changes in direction for the water flow that seem unlikely given the smooth topography and the lack of obstacles.

[14] Although less probable, more extreme reconstructions are possible. A minimum offset of 24 ± 2 m is obtained by realigning the risers F1/F2 on both sides of the fault (Figure 6b). This offset may be used to derive a maximum slip rate from the age of surface F1 and a minimum slip rate from the age of surface F2 [*Tapponnier et al.*, 2001; *van der Woerd et al.*, 2002; *Mériaux et al.*, 2005]. This reconstruction assumes that the riser F1/F2 has been constantly refreshed on both sides of the fault, erasing any offset accumulated before the abandonment of F1; otherwise, the offset is overestimated. In this configuration the position of the southern edge of the fan relative to C3 implies an unlikely oblique water flow to emplace F2 so far to the south, hardly compatible with the shape of the fan. In addition, the inferred apex of the fan would be far from the center of the channel. A maximum offset of 64 m is obtained by bringing the edges of the downstream fan F2 back in front of the rims of C3 (Figure 6c). Yet this reconstruction appears to be contradictory to the geomorphic interpretation of the radial incision pattern within surface F2 (Figure 5).

[15] Surface F2, located south of the mouth of channel C2, and the small remnant F2, located south of the mouth of channel C4 (Figure 3), are not preserved well enough for independent offset determination. Nevertheless, moving all downstream surfaces 48 m backward yields a consistent position of all of the patches of F2 relative to feeding channels, further supporting the best-offset reconstructions (Figure 6d).

[16] The remains of surface F3 west of the fault are scarce and not well preserved. They are of only little use in quantifying the left-lateral offset on the fault. We propose possible intervals for the offsets by adjusting the remains of F3 downstream from the fault trace with upstream channels. Such reconstructions correspond to the geometry of F3 when incision started. Accuracy is limited by uncertainties in the channel width east of the fault, which probably widened over time, and by the unknown initial extent of the patches of F3 west of the fault that have been laterally cut by active channels. Figure 7 presents the reconstructions for left-lateral offsets of 255 ± 8, 370 ± 18, 560 ± 60, and 680 ± 20 m that are equally satisfactory in terms of fitting surfaces across the fault. In the case of the 255 and 370 m reconstructions, the northern patch of F3 west of the fault would have been transported across one major channel, C2, while the two southern patches have crossed one or two channels, C5 and C6: channels, however, that do not seem as powerful as the northern channels based on the size of the fans F1 emplaced at their mouth (Figure 3). As for the larger reconstructions the northern patch of F3 would have to be transported across two major channels, C2 and C1. Given the scarce remains of F3 west of the fault, the water flow coming out of the channels seems to be able to erase the F3 deposits fairly efficiently. Thus, we would favor offsets of 255 ± 8 and 370 ± 18 m.

2.2. The Hamrat Al-Fidan Site

2.2.1. Setting and Geomorphic Mapping

[17] The Hamrat Al-Fidan site lies in the northern Araba Valley (Figure 1b). There, the fault is located at the eastern

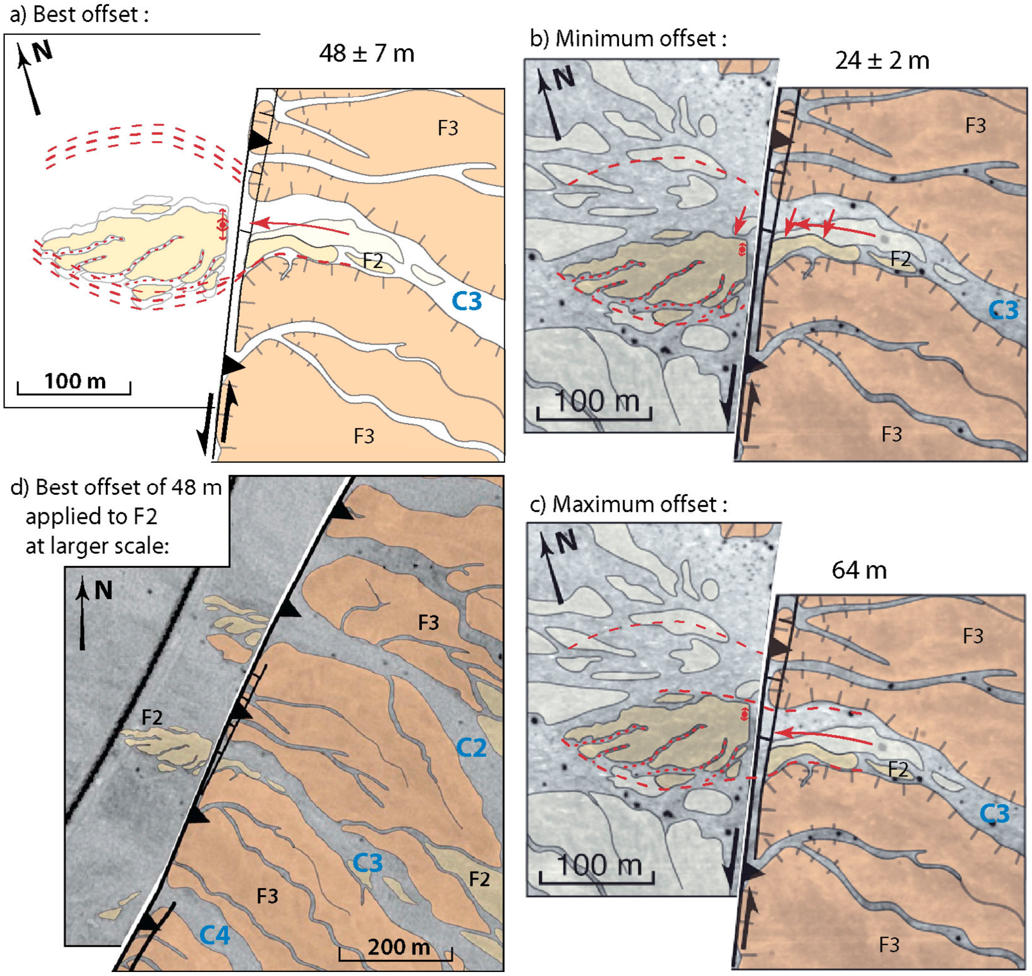

Figure 6. Tectonic reconstructions of alluvial fan F2 at the Jabal Al-Muhtadi site. The red arrow within the stream bed of C3 indicates the axis of channel C3. (a) Dashed red lines indicate the restored position of fan surface F2 at the mouth of channel C3 and the shape of its southern edge across the fault. Thick dashed lines refer to the central value of the offset and thin dashed lines refer to the lower and upper bounds. (b) Red arrows point to the riser F2/F1. (c) Thick dotted lines indicate the edge of fan surface F2 matched with the banks of C3. Both Figure 6b and Figure 6c are contradictory to the geomorphic interpretation of fan surface F2 (Figure 6d; see text).

edge of the valley (Figure 8). The fault trace is complex owing to two successive steps to the east that produce restraining bends, where intensively fractured Cretaceous bedrock [*Rabb'a*, 1994] crops out through sand dunes and a bajada sloping (~1°) toward the northwest.

[18] Between the two push-up structures, two parallel fault branches, $\varphi 1$ and $\varphi 2$, accommodate left-lateral displacement. Fault $\varphi 1$, with the longest continuous trace and where numerous offset gullies have been observed [*Klinger et al.*, 2000b], appears to be the main active fault. Fault azimuth changes from N7°E in the south to N15°E in the north. A subsiding basin filled with light-colored recent deposits attests to some transtensional motion in the south (Figure 9), while, in the north a compressive component uplifts alluvial deposits, later incised, and brings Cretaceous bedrock to the surface.

[19] An incised dark alluvial surface, clearly visible on satellite images, is cut and displaced left laterally by the faults (Figures 8 and 9). This abandoned bajada is formed by coalescent alluvial deposits originating from a few small drainages coming down the nearby rocky range, the Jabal Hamrat Fidan, composed of Precambrian granite [*Rabb'a*, 1994]. The largest catchment is about 1 km^2 (Figure 8). On the basis of the surface height above the active streams, surface darkness, and degree of incision, we identified four successive alluvial surfaces (Figure 9).

[20] East of fault $\varphi 1$, a dark and deeply incised surface, F4, is prominent (Figures 9 and 10a). Three lower surfaces are also observed: F3, F2, and F1. Surface F4 lies about 2 to 4 m above the active streams. At some places, it has been incised by regressive gullies (Figure 10a), significantly affecting the preservation of the flat top part of the surface. Two main channels, C1 and C2, incised the various surfaces. While channel C2 is fairly wide (~60 m between fault $\varphi 1$ and fault $\varphi 3$), C1 is only 15 to 20 m wide, widening up to 25 m at fault $\varphi 1$, with banks well defined by sharp incision in F4.

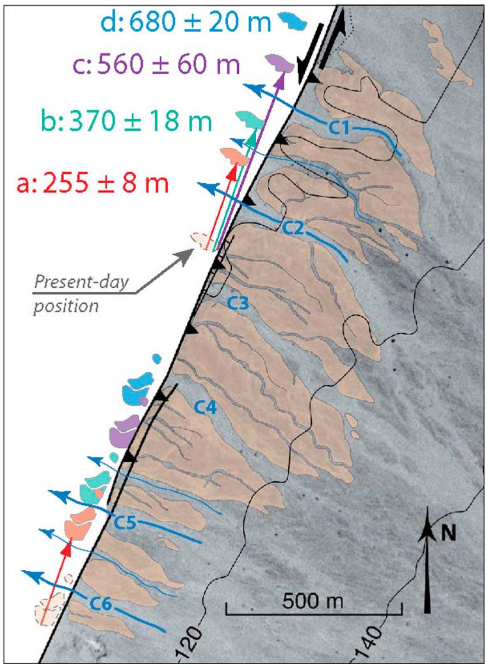

Figure 7. Four possible reconstructions of F3 at the Jabal Al-Muhtadi site. Reconstructions a and b are the most reasonable, while the larger offsets c and d are less likely, as they require the northern patch of F3 to pass in front of two major channels (C1 and C2) that could have eroded it away (see text).

[21] West of fault φ2, from north to south, the surfaces become darker and, thus, may be older (Figures 9 and 10b). The darkest surfaces have been mapped as F4, based on their similar color and relative level above the active channels to surface F4 east of the fault. Surface F4 is incised by a main channel, C1′, similar in width (25 to 30 m) to channel C1 east of the fault. The surface located north of channel C1′ looks smoother and lighter in the satellite views compared to the southern one. In the field, however, we could not find any significant difference in surface appearance or in the height of the two surfaces across the channel. Hence, both surfaces are considered to be part of the same unit.

[22] North of F4, west of the fault, a surface that is lighter in color, mapped as F3, does not extend as far to the west as F4 and is separated from F4 by a straight channel, suggesting incision and lateral cutting of F4 prior to the deposition of F3. Contrary to F4, cobbles are sparse on surface F3, which is mostly composed of pebbles. F3-like surfaces are observed continuously farther to the north, crossed only by a few minor channels. Fractured Cretaceous limestone locally crops out along the secondary fault φ4 (Figure 10b).

[23] In the northern part of the site, west of the fault, an alluvial surface, mapped F2, is inset in F3 (Figure 10b); surface F3 had been incised by a major channel later infilled by unit F2. The width of surface F2, ~48 m at fault φ2 and ~38 m at fault φ4, provides constraints on the width of the feeding channel. The inset surface F2 could be mapped continuously across fault φ2 and up to the main left-lateral fault φ1. At present, F2 abuts onto surface F4 across the fault φ1, showing that it has been disconnected from its source owing to the fault activity. Similarly, the narrow channel C2′, incised in F2, could be followed continuously across φ2 and up to φ1, but it is beheaded east of φ1 and it is now abandoned. F2 and channel C2′ are not, or are barely, affected by fault motion along φ2, or φ4, confirming that φ1 is the main strike-slip branch.

[24] Lower and lighter surfaces, mapped as F1, could be observed only at the mouth of channel C3′. Other F2 and F1 types of surfaces can be identified in the distal part of the bajada.

[25] Between the two sub-parallel faults φ1 and φ2, we observed four levels of alluvial deposits. Their height above the present-day streams increases from north to south, as well as their darkness (Figures 9 and 10b). The continuity of F2 across fault φ2 ensures surface correlation.

2.2.2. Offset Measurements

[26] As already described, the abrupt ending of surface F2 and channel C2′ against φ1 and abutting onto F4 shows that they have been disconnected from their feeder, the width of which should be ~40 m or less, given the morphology of F2. Only two sources are possible for F2: channels C1 and C2 (Figure 9). The width of C1 matches the width of F2 at fault φ1, while channel C2 is too wide and can be discarded. Bringing the inset surface F2 back in front of the outlet of channel C1 yields an offset of 160 ± 8 m (Figure 11). This offset applies to channel C2′ as well, showing that F2W was already incised when it was disconnected from its source and that the incision event occurred shortly after the surface was abandoned. This reconstruction also realigns two gullies, S1 and S2′, across φ1.

[27] To determine the offset of surface F4, we propose to match channel C1 with channel C1′ (Figure 12), as they have very similar widths. The channel banks, well defined on both sides of the fault, are used as piercing lines to retrieve the original shape of the channel. At fault φ1 the banks of channel C1 are oriented E-W, attesting to a westward orientation of the water flow. At fault φ2 the southern bank of C1′ is oriented E-W too, but the northern bank is oriented ENE-WSW. This suggests a W to WSW orientation for the water flow that enters C1′. One should keep in mind the possible modification in the geometry of the channel banks of C1′ close to fault φ2, due to lateral erosion and displacement of C1′ toward the south relative to its upstream sources. The lack of constraints between fault φ1 and fault φ2 also leaves some uncertainty in the reconstructions.

[28] Considering a westward water flow at the mouth of C1 and a water flow varying between ENE-WSW (Figure 12a) and E-W (Figure 12b) at the head of C1′, the reconstruction of channel C1-C1′ leads to an offset of 626 ± 37 m. Some freedom remains regarding the position of the block located between faults φ1 and φ2. We chose to align the northern risers of F4 on each block across the faults. This alignment could correspond to the incision of channel C2 in F4, synchronous with the incision of C1-C1′. The two reconstructions are also consistent with the general shape of surface F4. West of the fault, F4 extends more to the south than to the east of the fault, which could be explained by the local slope oriented WSW. Eventually, a maximum bound of 737 m for the offset is obtained by realigning the southern extent of the surface on both sides of the fault (Figure 12c). In this configuration, however, the continuity of channel C1-C1′ could hardly be restored.

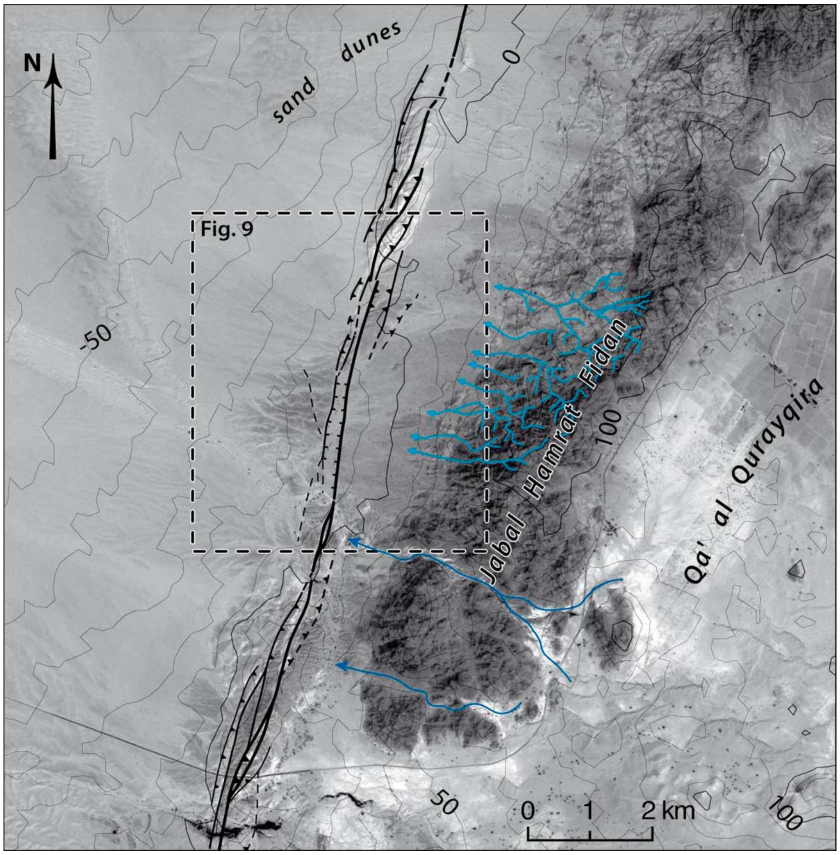

Figure 8. SPOT5 satellite overview of the Hamrat Al-Fidan site. Topographic contour lines from SRTM3 data (negative altitudes are below sea level). Dark blue lines indicate the only two drainages that cross the Jabal Hamrat Fidan ridge at present. Light blue lines represent the drainage network at the origin of the offset bajada.

[29] Surface F3 could not be used to get any further information about the left-lateral displacement along the fault owing to the lack of geomorphic markers on this surface.

3. Surface Exposure Dating

3.1. Analytical Approach

[30] Abandoned alluvial surfaces can be dated using cosmogenic surface exposure dating. Exposure of clasts to cosmic rays induces the production of cosmogenic isotopes (e.g., ^{3}He, ^{10}Be, ^{21}Ne, ^{36}Cl) within the clast minerals, some of these isotopes being radioactive [*Lal*, 1991; *Gosse and Phillips*, 2001]. In this study we use ^{10}Be CRN, produced from silicon and oxygen atoms of quartz-rich rock types.

[31] The number $N_{10\mathrm{Be}}$ of ^{10}Be isotopes within a rock sample as a function of time t and depth z is given by equation (1) [*Lal*, 1991]:

$$N_{10\mathrm{Be}(t,z)} = N_{10\mathrm{Be}(t,0)} + [P\exp(-\mu z)/(\lambda+\mu\varepsilon)]\{1-\exp[-(\lambda+\mu\varepsilon)t]\}, \quad (1)$$

where $N_{10\mathrm{Be}(\mathrm{t},0)}$ represents the number of atoms in the rock sample inherited from possible exposure prior to its final deposition, P is the production rate of ^{10}Be (at/g of quartz/a), λ is the half-life of ^{10}Be, μ is the ratio of the sediment density and the attenuation length of cosmic rays, and ε is the erosion rate of the alluvial surface.

[32] To reduce the number of parameters that intervene in equation (1), we work under two hypotheses. First, we assume that exposure during transport and temporary storage of samples in the drainage basin is negligible. This assumption has to be reconsidered for each new site according to the area of the drainage basin. The age distribution obtained from multiple samples from the same surface may enable one to detect such a bias [*Van der Woerd et al.*, 2006]. Second, we assume that the erosion rate is likely to be low, owing to the arid climate in this area. This assumption is supported by the development of desert varnish and by desert pavement that protects the surface from deflation [*Wells et al.*, 1995; *Quade*, 2001; *Regard et al.*, 2006; *Van der Woerd et al.*, 2006]. Later in this section we estimate analytically the maximum erosion rate and discuss its effect on the ages. Under these assumptions and considering samples collected on the ground surface, equation (1) simplifies to equation (2):

$$N_{10\mathrm{Be}(0,t)} = (P/\lambda)[1-\exp(-\lambda t)]. \quad (2)$$

[33] Sample processing consists of isolating the quartz grains from the rock samples and cleaning them from meteoric contamination following the chemical protocol of *Kohl and Nishiizumi* [1992]. Next, cleaned quartz samples

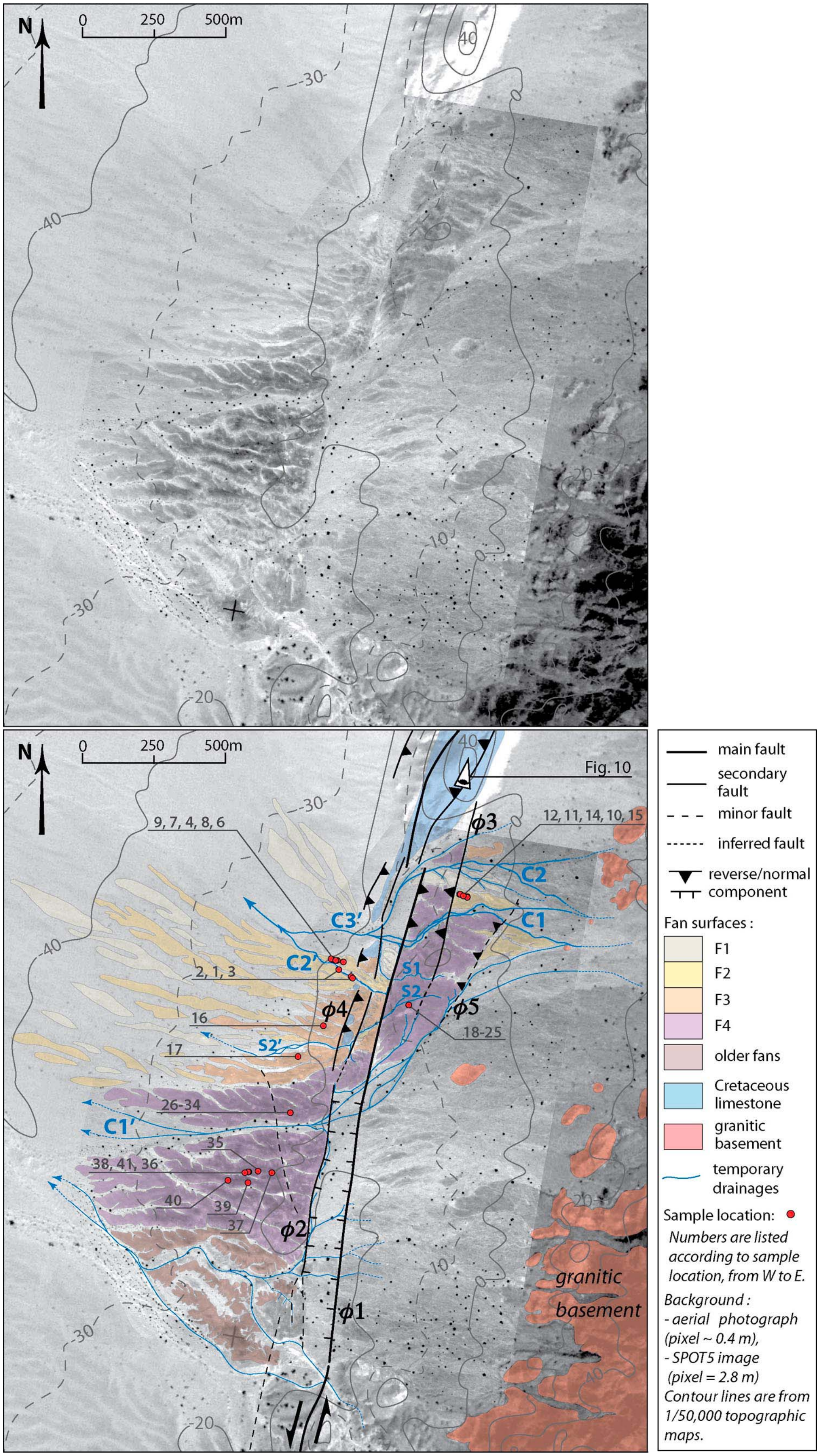
N
0
250
500m
-30-
40
-40-
-20-
-10-
-30-
-20-
Fig. 10
9, 7, 4, 8, 6
12, 11, 14, 10, 15
φ3
C2
C3'
C1
C2'
2, 1, 3
S1
S2
φ4
φ5
16
18-25
S2'
17
26-34
C1'
35
38, 41, 36
40
39
37
φ2
φ1
granitic basement
main fault
secondary fault
minor fault
inferred fault
reverse/normal component
Fan surfaces :
F1
F2
F3
F4
older fans
Cretaceous limestone
granitic basement
temporary drainages
Sample location: ●
Numbers are listed according to sample location, from W to E.
Background :
- aerial photograph (pixel ~ 0.4 m),
- SPOT5 image (pixel = 2.8 m)
Contour lines are from 1/50,000 topographic maps.

Figure 9

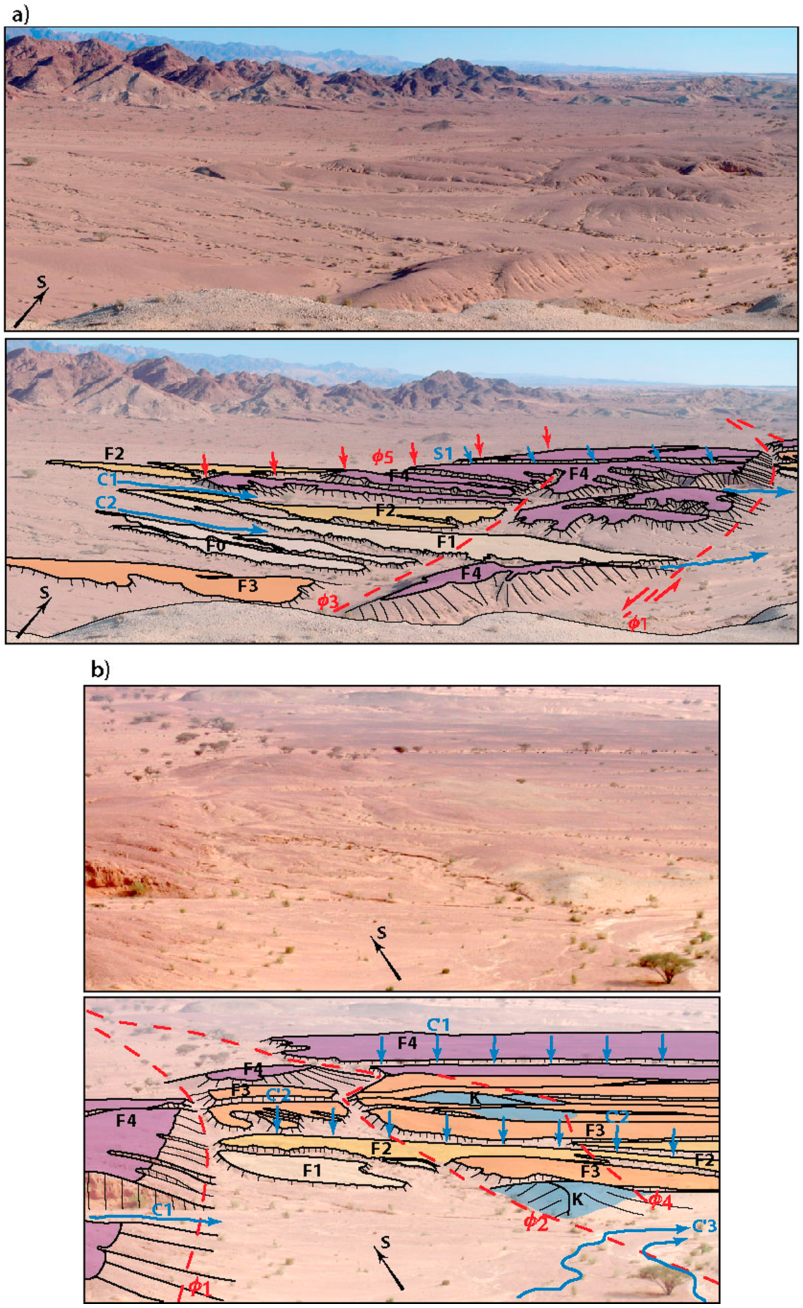

Figure 10. Field views and morphotectonic interpretations at the Hamra Al-Fidan site. Dotted red lines and red arrows indicate the fault trace and blue arrows point to drainages. (a) View of the alluvial surfaces east of fault $\varphi1$. (b) View of the alluvial surfaces located between fault $\varphi1$ and fault $\varphi2$ and west of fault φ 2. K: Cretaceous bedrock knob.

are dissolved in hydrofluoric acid, after the addition of a ^{9}Be spike solution. We then separate the atoms of beryllium by anion and cation exchange chromatography. We precipitate beryllium hydroxides and ignite them to obtain beryllium oxide. Finally, the ^{10}Be/^{9}Be ratio is measured by accelerator mass spectrometry (AMS) at the Lawrence Livermore National Laboratory AMS facility [*Davis et al.*, 1990; *Finkel and Suter*, 1993] and normalized to the KNSTD3110 standard (see Tables 2a, 2b, and 2c). ^{10}Be CRN model ages were calculated following equation (2) and using the online CRONUS-Earth calculator and the scaling scheme “St” of *Balco et al.* [2008]. This scheme uses the constant-over-time scaling factors of *Lal* [1991], the rescaling as functions of latitude and atmospheric pressure by *Stone* [2000], and

Figure 9. Aerial photograph superimposed on SPOT5 image at the Hamrat Al-Fidan site and morphotectonic map. We mapped the alluvial surfaces and the fault trace from field observations, stereoscopic aerial photos, high-resolution Google Earth images, and SPOT5 images. The relative age of alluvial surfaces increases from F1 to F4.

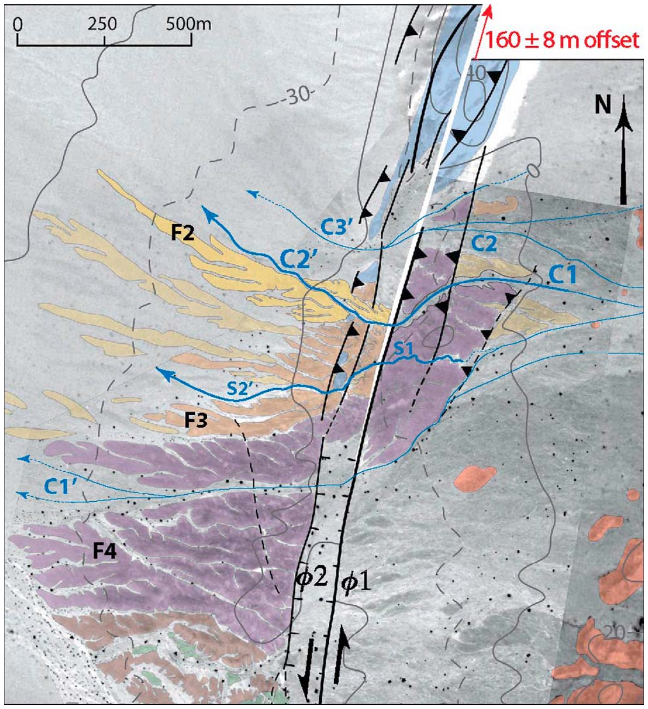

Figure 11. Tectonic reconstruction of the inset surface F2 and abandoned channel C2′ at the mouth of channel C1, at the Hamrat Al-Fidan site. The reconstruction also restores stream S1–S2′.

the revised production rate of 4.96 ± 0.43 atoms/g annually [*Balco et al.*, 2008].

[34] On each alluvial surface we have collected several samples, well embedded in the surface (Figures 13 and 15), to ensure their long-term stability [e.g., *Ryerson et al.*, 2006]. We preferentially sampled granitic cobbles because they were the most representative clast size and lithology on our surfaces of interest. Amalgamated samples of 10 to 20 granitic or quartz pebbles of similar size were collected in parallel, when available. Such samples are expected to represent an average of the clast population and may help gain a better understanding of the exposure history of the clasts by comparison of their age with that of individual cobbles [*Hetzel et al.*, 2002; *Matmon et al.*, 2009].

[35] At each sampling site the horizon was surveyed to estimate the shielding of cosmic rays related to the surrounding topography. The shielding correction was found to be negligible for all samples.

[36] To calculate a maximum erosion rate, we used samples collected on old terrace levels (the ages of which are known to be ≥300 ka [*Le Béon*, 2008]) at two sites in the Wadi Araba, Mazla and Jabal Al-Risha (Figure 1b, Table 1).

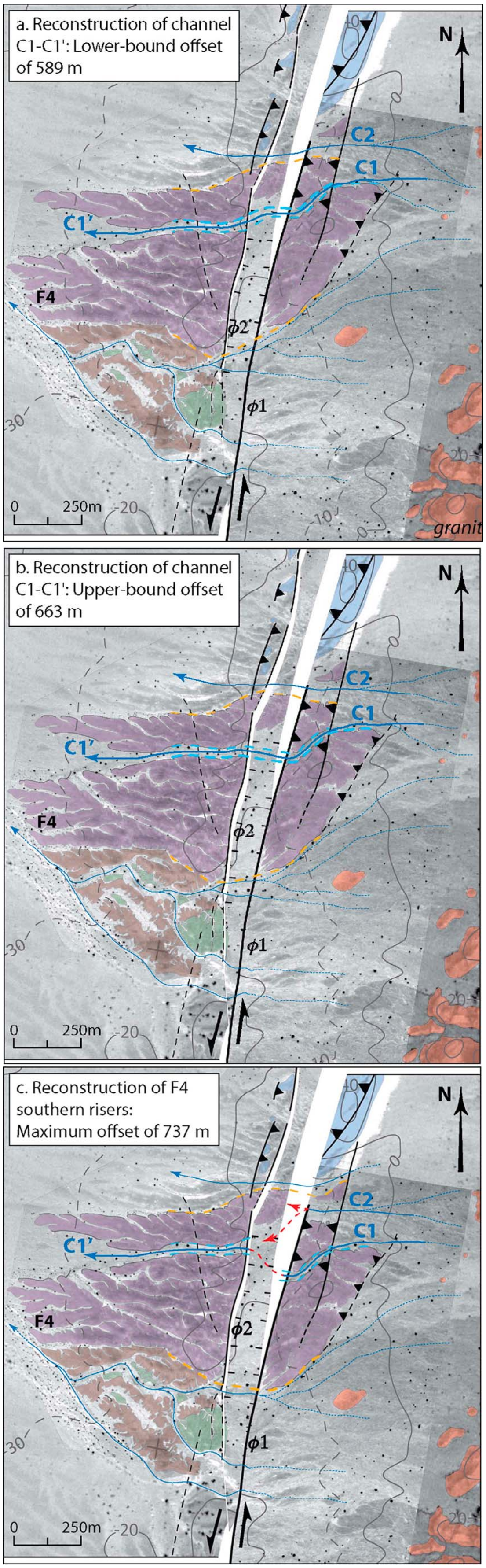
a. Reconstruction of channel C1-C1': Lower-bound offset of 589 m

b. Reconstruction of channel C1-C1': Upper-bound offset of 663 m

c. Reconstruction of F4 southern risers: Maximum offset of 737 m

Figure 12. Tectonic reconstructions of the offset surface F4, at the Hamrat Al-Fidan site. (a, b) Reconstruction of channel C1-C1′ incised in F4. The thick dotted blue line indicates the piercing line used for each reconstruction. The parallel thin dotted blue line corresponds to the opposite bank of the reconstructed channel. (c) Reconstruction based on the southern risers of F4. Red arrows indicate the difficulty in reconstructing the channels in this configuration.

Figure 13. Sampling surface F2 at the Jabal Al-Muhtadi site. (a) View of surface F2 east of the fault, within channel C3. (b) Collecting a well-embedded cobble on surface F2 upstream (sample JM06-3; Tables 2a, 2b, and 2c).

We assumed that enough terrace material has been removed by erosion to justify the steady-state erosion model [*Lal*, 1991] (i.e., production is balanced by radioactive decay) for the samples with the highest ^{10}Be concentrations. We obtained an average maximum erosion rate of 2.1 ± 0.1 m/Ma (Table 1). Because the study area experiences uniform climatic conditions and because the configurations of the four sites are similar (gentle slopes, sites isolated from the relief), we can reasonably apply the same maximum erosion rate at the sites presented here. This clearly is a conservative approach, as an extremely low maximum erosion rate of 0.3 m/Ma has been measured in the neighboring Paran Plains of Israel by *Matmon et al.* [2009]. We found no evidence in the field of significant surface deflation (such as shallow-rooted or uprooted cobbles or lighter varnish at the cobble base) or of erosion of the desert varnish on the cobbles.

[37] Minimum and maximum ages (calculated assuming no erosion and maximum erosion, respectively) are listed in Tables 2a, 2b, and 2c. The effect of the maximum erosion rate remains negligible for most samples, confirming the zero-erosion hypothesis [e.g., *Ryerson et al.*, 2006]. For ages of the order of 100 ka, maximum erosion would lead to a 15% increase in age, which is barely larger than uncertainty.

[38] CRN dating of alluvial surfaces may be biased not only by preexposure and erosion, but also by the complexity of alluvial processes (e.g., duration of surface activity, postdepositional contamination related to exceptional flood events). All such processes may result in a scattered age distribution. The definition of age clusters and the rejection of outliers are often controversial, especially in small data sets, and depend in large part on the sample distribution, which may, or may not, appear Gaussian. Typically, outliers are defined by visual rejection [e.g., *Van der Woerd et al.*, 1998] or by using Chauvenet's criterion [*Mériaux et al.*, 2004, 2009]. The age of each cluster is routinely reported as the mean or the weighted mean of the cluster, although other authors have used the "oldest-age method" [e.g., *Briner et al.*, 2005] or considered the interval covered by all of the ages [e.g., *Ritz et al.*, 2006]. In this study, after preliminary statistical tests [*Le Béon*, 2008], we eventually rejected visually obvious outliers. For each surface we calculated, from the minimum CRN model ages, the weighted mean age, applying weights that depend on the normalized internal uncertainty, and the standard deviation σ. We discuss specific cases in which scattered data are not all covered by the interval mean ± σ and we propose using a wider interval as a conservative age estimate.

Table 1. Maximum Erosion Rates Derived From Samples Collected on Old Alluvial Surfaces at the Jabal Al-Risha and Mazla Sites in the Wadi Araba

Site[a]	Sample	Lithology[b]	Elev. (m)	^{10}Be		Erosion Rate[c]	
				(at/g qtz)	(±)	(m/Ma)	(±)
Jabal Al-Risha							
(N30.233, E35.21)	RA06-36	qtzite	251	1,396,001	32,856	2.21	0.21
	RA06-38C	a. qtz	251	1,458,867	34,260	2.23	0.21
Mazla							
(N30.377, E35.261)	RA06-35	qtzite	251	1,600,924	37,535	1.89	0.18
	MA06-12C	a. qtz	196	1,439,213	45,699	2.17	0.21
	MA06-11	qtzite	196	1,443,200	43,123	2.08	0.20
	MA06-9	qtzite	196	1,449,812	42,101	2.02	0.20
	MA06-10	rhyo	197	1,606,357	38,331	1.94	0.19
Mean						2.08	0.13

[a] Location shown in Figure 1b.

[b] aa. qtz, amalgamated quartz sample; elev., elevation; qtzite, quartzite; rhyo, rhyolite; ±, analytical uncertainty. Geomorphic analysis and exposure dating data are detailed by *Le Béon* [2008].

[c] Erosion rates were computed using the online calculator of *Balco et al.* [2008] (available at http://hess.ess.washington.edu/).

Table 2a. ^{10}Be CRN Dating: Sample Descriptions and Analytical Parameters

Surface	No.[a]	Sample	Lithology[b]	Location (°N/°E)	Elevation (m)[c]	Thickness (cm)	Thickness Scaling Factor
Jabal Al-Muhtadi site							
F2E	3	JM06-3	Gr	29.742203/35.045387	106	7.5	0.9393
	4	JM06-4	Gr	29.742169/35.045341	106	5.5	0.9550
	1	JM06-1	Gr	29.742059/35.045243	106	6	0.9510
F2W	2	JM06-2	Gr	29.742137/35.045339	106	6	0.9510
	7	JM05-4	Gr	29.742083/35.044555	103	5	0.9590
	8	JM05-5	Gr	29.742083/35.044555	103	7	0.9432
	6	JM05-3	Gr	29.742083/35.044555	103	9	0.9278
	5	JM05-1 & -2	Qtz	29.742083/35.044555	103	3.5	0.9710
	9	JM05-7	Gr	29.742083/35.044555	103	4	0.9670
	—	JM05-6	Gr	29.742083/35.044555	103	—	
F3E	10	JM06-5A	a. gr	29.741669/35.045534	109	2	0.9833
	11	JM06-5B	a. qtz	29.741669/35.045534	109	2	0.9836
Hamrat Al-Fidan site							
F2E	10	FD06-5	Gr	30.632477/35.352392	−3	5	0.9590
	11	FD06-9	Qtz	30.632546/35.352151	−2	3	0.9756
	12	FD06-10A	a. gr	30.632513/35.352252	−2	2	0.9833
	13	FD06-8	Gr	30.632566/35.352135	−3	9	0.9278
	14	FD06-7	Gr	30.632513/35.352252	−2	10	0.9202
	15	FD06-6	Gr	30.632454/35.352399	0	5	0.9590
F2W	4	FD06-19	Gr	30.630666/35.347828	−12	3	0.9751
	5	FD06-22A	a. gr	30.630666/35.347828	−13	3	0.9751
	6	FD06-17	Gr	30.630614/35.348092	−12	6	0.9510
	7	FD06-20	Gr	30.630702/35.347729	−14	7	0.9432
	8	FD06-18	Gr	30.630674/35.347878	−14	4	0.9670
	9	FD06-21	Gr	30.630718/35.347666	−13	6	0.9510
Abandoned channel	—	FD06-24	Gr	30.630400/35.348001	0	—	—
	1	FD06-25	Gr	30.630190/35.348336	−2	4	0.9670
	2	FD06-23	Gr	30.630404/35.347940	1	6	0.9510
	3	FD06-26	Gr	30.630132/35.348401	−2	4.5	0.9630
F3W(N)	16	FD05-1	a. qtz	30.628750/35.347361	−21	3	0.9756
F3W(S)	17	FD05-2	a. qtz	30.627833/35.346472	−21	3	0.9756
F4W(S)	35	FD06-28	Gr	30.624466/35.345027	−17	4	0.9670
	36	FD06-29	Gr	30.624458/35.344697	−17	5.5	0.9550
	37	FD06-27	Gr	30.624422/35.345491	−14	4	0.9670
	38	FD06-31	Gr	30.624441/35.344570	−17	4	0.9670
	39	FD06-33	Gr	30.624128/35.344656	−18	3	0.9751
	40	FD06-32	Gr	30.624219/35.343985	−18	5	0.9590
	41	FD06-30	Gr	30.624450/35.344686	−18	3	0.9751
F4W(N)	26	FD03-1	Gr	30.626194/35.346167	−20	5.5	0.9550
	27	FD03-2	Gr	30.626194/35.346167	−20	5	0.9590
	28	FD03-5	Gr	30.626194/35.346167	−20	3	0.9751
	29	FD03-3	Gr	30.626194/35.346167	−20	5	0.9590
	30	FD03-4	Gr	30.626194/35.346167	−20	4	0.9670
	31	FD03-4bis	Gr	30.626194/35.346167	−20	3.5	0.9710
	32	FD03-8B/C	a. qtz	30.626194/35.346167	−20	2.5	0.9796
	33	FD03-6	Gr	30.626194/35.346167	−20	4	0.9670
	34	FD03-7	Gr	30.626194/35.346167	−20	4.5	0.9630
F4E	—	FD03-11	Gr	30.629305/35.350305	−11		
	18	FD03-10	Gr	30.629305/35.350305	−11	4	0.9670
	19	FD03-13	Gr	30.629305/35.350305	−11	4	0.9670
	20	FD03-15	Gr	30.629305/35.350305	−11	6.5	0.9471
	21	FD03-12	Gr	30.629305/35.350305	−11	5	0.9590
	22	FD03-9	Gr	30.629305/35.350305	−11	6	0.9510
	23	FD03-14	Gr	30.629305/35.350305	−11	5	0.9590
	24	FD03-16	Gr	30.629305/35.350305	−11	5.5	0.9550
	25	FD03-17B/C	a. qtz	30.629305/35.350305	−11	2.5	0.9796

[a] No. corresponds to the number used in maps and graphs.

[b] a. gr, amalgamated granite sample; a. qtz, amalgamated quartz sample; Gr, granite; Qtz, quartz. Densities of 2.7 and 2.65 g/cm^3 were used for granitic samples and pure quartz samples, respectively.

[c] Elevation in meters above sea level; negative elevations are below sea level.

Table 2b. ^{10}Be CRN Dating: Analytical Parameters and ^{10}Be/^{9}Be Ratios

Surface	No.	Background[a]	Yearly Production Rate by Spallation (atoms/g)	Yearly Production Rate by Muons (atoms/g)	Shielding Factor	Mass Quartz (g)	Mass Carrier (g)	^{10}Be/^{9}Be	
								($\times 10^{-14}$)[b]	(±)
Jabal Al-Muhtadi site									
F2E	3	*	3.80	0.185	0.99965	30.4308	0.2517	7.42	0.29
	4	*	3.86	0.185	0.99965	30.3059	0.2521	10.38	0.24
	1	*	3.85	0.185	0.99965	30.3469	0.2501	21.50	0.51
F2W	2	*	3.85	0.185	0.99965	29.1236	0.2499	28.41	0.67
	7	**	3.87	0.185	0.99931	10.3708	0.1222	2.67	0.35
	8	**	3.81	0.184	0.99931	10.2495	0.1086	5.13	0.48
	6	**	3.74	0.184	0.99931	10.0485	0.1214	4.61	0.34
	5	**	3.92	0.185	0.99931	10.5729	0.1227	8.38	0.46
	9	**	3.90	0.185	0.99932	12.516	0.1218	11.88	0.5
	—	—	—	—	—	—	[c]	—	—
F3E	10	*	3.99	0.186	0.99962	30.0913	0.2552	33.55	0.80
	11	*	3.99	0.186	0.99962	30.4032	0.2542	47.91	1.12
Hamrat Al-Fidan site									
F2E	10	*	3.59	0.178	0.99922	20.2564	0.249	7.64	0.28
	11	*	3.65	0.179	0.99922	20.5567	0.2474	14.82	0.38
	12	*	3.68	0.179	0.99922	20,2656	0.248	17.36	0.49
	13	*	3.47	0.178	0.99922	20.461	0.2481	16.11	0.64
	14	*	3.45	0.178	0.99922	5.0804	0.2479	4.64	0.30
	15	*	3.60	0.178	0.99922	20.2515	0.2477	24.39	0.61
F2W	4		3.62	0.178	0.99991	12.6965	0.2494	15.82	0.31
	5	*	3.62	0.178	0.99991	17.6126	0.2493	30.09	0.65
	6	*	3.54	0.178	0.99991	20.0425	0.2482	42.87	1.04
	7	*	3.50	0.177	0.99991	20.4535	0.2494	44.29	1.83
	8	*	3.59	0.178	0.99991	4.7305	0.2508	11.29	0.32
	9	*	3.53	0.178	0.99991	14.0789	0.2487	37.70	1.52
Abandoned channel	—	—	—	—	—	—	[c]	—	—
	1	*	3.63	0.178	0.99974	30.2123	0.2476	34.82	0.82
	2	*	3.58	0.178	0.99974	30.6305	0.2466	35.27	0.92
	3	*	3.61	0.178	0.99974	27.295	0.2503	56.28	1.31
F3W(N)	16	**	3.60	0.177	0.99991	10.2078	0.1222	37.31	1.03
F3W(S)	17	**	3.60	0.177	0.99991	10.2155	0.1226	28.84	0.82
F4W(S)	35	*	3.58	0.178	0.99975	9.2663	0.2482	17.02	0.35
	36	*	3.53	0.177	0.99975	13.6247	0.2476	27.54	0.53
	37	*	3.59	0.178	0.99975	4.9072	0.2462	11.88	0.38
	38	*	3.58	0.178	0.99975	11.8172	0.246	29.44	1.07
	39	*	3.61	0.178	0.99975	15.1313	0.2459	39.65	0.88
	40	*	3.55	0.177	0.99975	12.8968	0.2468	33.37	0.81
	41	*	3.61	0.178	0.99975	13.8202	0.2467	43.22	0.83
F4W(N)	26	#	3.53	0.177	0.99975	10.7703	0.3919	16.03	0.47
	27	#	3.54	0.177	0.99975	14.1203	0.406	22.63	0.60
	28	#	3.60	0.178	0.99975	3.1588	0.4127	6.41	0.33
	29	#	3.54	0.177	0.99975	4.8605	0.3602	11.79	0.62
	30	#	3.57	0.177	0.99975	15.5243	0.3957	35.52	0.92
	31	#	3.58	0.177	0.99975	16.4426	0.4088	37.91	0.93
	32	**	3.62	0.178	0.99975	16.068	0.127	70.67	2.04
	33	#	3.57	0.177	0.99975	8.4432	0.393	30.63	0.96
	34	**	3.56	0.177	0.99975	10.1874	0.112	63.76	5.71
F4E	—	—	—	—	—	—	[d]	—	—
	18	**	3.60	0.178	0.99991	9.8686	0.1039	20.00	0.74
	19	#	3.60	0.178	0.99991	9.1432	0.4151	15.22	0.60
	20	#	3.52	0.178	0.99991	16.311	0.4122	37.58	1.19
	21	#	3.57	0.178	0.99991	15.4856	0.3755	41.62	1.02
	22	#	3.54	0.178	0.99991	19.0782	0.404	49.82	1.21
	23	#	3.57	0.178	0.99991	17.2733	0.4179	47.47	1.16
	24	#	3.55	0.178	0.99991	13.9514	0.4116	41.37	1.02
	25	#	3.64	0.178	0.99991	15.3942	0.4102	49.71	1.70

[a] Background correction using the following blank values: (*) $1.7655 \times 10^{-15} \pm 9.2861 \times 10^{-16}$; (**) $4.7376 \times 10^{-15} \pm 2.6248 \times 10^{-16}$; (#) $2.0669 \times 10^{-14} \pm 5.5274 \times 10^{-16}$.

[b] Ratios have been normalized to the KNSTD3110 standard prepared by *Nishiizumi et al.* [2007], with a ^{10}Be/^{9}Be ratio of 2.85×10^{-12}.

[c] Low current at the AMS (accelerator mass spectrometer).

[d] Too little material left after leaching.

Table 2c. ^{10}Be CRN Dating: ^{10}Be Concentrations and Model Ages[a]

Surface	No.	^{10}Be Conc.						
		(atoms/g SiO_2 × 10^4)	(±)	Min. Age[b]	Int. ±[c]	Ext. ±[d]	Max. Age[e]	Ext. ±[d]
Jabal Al-Muhtadi site								
F2E	3	4.10	0.16	10.32	0.40	0.99	10.50	1.02
	4	5.77	0.14	14.31	0.34	1.29	14.66	1.36
	1	11.84	0.28	29.58	0.71	2.68	31.16	2.99
F2W	2	16.29	0.39	40.82	0.98	3.71	43.93	4.32
	7	1.87	0.25	4.61	0.61	0.73	4.64	0.74
	8	3.23	0.30	8.12	0.77	1.04	8.23	1.07
	6	3.31	0.25	8.44	0.63	0.97	8.56	0.99
	5	5.78	0.31	14.13	0.77	1.45	14.48	1.53
	9	3.23	0.30	16.88	0.72	1.64	17.38	1.74
	—	—						
F3E	10	19.01	0.46	46.09	1.12	4.20	50.12	5,00
	11	26.77	0.63	65.19	1.55	5.96	73.51	7.68
Hamrat Al-Fidan site								
F2E	10	6.28	0.23	16.723	0.626	1.587	17.212	1.684
	11	11.92	0.31	31.341	0.819	2.864	33.092	3.205
	12	14.20	0.40	37.109	1.065	3.424	39.652	3.929
	13	13.06	0.52	36.081	1.453	3.481	38.473	3.977
	14	15.14	0.99	42.214	2.787	4.637	45.54	5.431
	15	19.93	0.50	53.498	1.353	4.901	59.019	6.02
F2W	4	20.77	0.40	55.398	1.094	5.002	61.354	6.194
	5	28.46	0.61	76.354	1.67	6.966	88.385	9.495
	6	35.47	0.86	97.922	2.438	9.056	119.091	13.776
	7	36.09	1.49	100.652	4.267	9.934	123.212	15.337
	8	40.01	1.13	109.195	3.164	10.254	136.577	16.618
	9	44.50	1.80	123.72	5.165	12.236	160.735	21.646
Abandoned channel	—	—						
	1	19.07	0.45	50.776	1.212	4.629	55.714	5.62
	2	18.98	0.49	51.219	1.353	4.706	56.247	5.724
	3	34.49	0.81	93.236	2.231	8.589	112.153	12.746
F3W(N)	16	26.53	0.73	55.219	1.599	5.121	61.006	6.308
F3W(S)	17	20.56	0.59	71.54	2.003	6.638	81.717	8.789
F4W(S)	35	30.46	0.63	82.827	1.746	7.553	97.263	10.626
	36	33.45	0.65	92.271	1.831	8.408	110.722	12.412
	37	39.83	1.26	108.721	3.549	10.338	135.82	16.709
	38	40.95	1.49	112.14	4.213	10.874	141.318	17.928
	39	43.06	0.96	117.251	2.682	10.832	149.756	18.417
	40	42.68	1.03	118.14	2.947	10.98	151.212	18.763
	41	51.55	0.99	141.231	2.801	13.025	192.968	25.934
F4W(N)	26	16.76	0.49	50.41	1.547	4.697	55.267	5.693
	27	18.70	0.50	50.96	1.367	4.688	55.932	5.695
	28	24.05	1.24	64.715	3.391	6.645	73.06	8.577
	29	25.10	1.32	68.714	3.668	7.096	78.226	9.327
	30	26.02	0.67	70.69	1.859	6.523	80.821	8.654
	31	27.08	0.67	73.339	1.842	6.747	84.333	9.064
	32	33.18	0.96	89.475	2.644	8.38	106.289	12.094
	33	40.97	1.28	112.505	3.625	10.691	141.908	17.664
	34	41.64	3.73	114.861	10.592	14.756	145.759	24.723
F4E	—	—						
	18	12.51	0.46	33.412	1.241	3.179	35.452	3.595
	19	19.85	0.79	53.299	2.144	5.16	58.778	6.332
	20	27.29	0.87	75.134	2.43	7.083	86.724	9.595
	21	29,00	0.71	78.983	1.977	7.274	91.951	10.041
	22	30.31	0.74	83.311	2.064	7.675	97.929	10.822
	23	33.00	0.80	90.139	2.245	8.321	107.635	12.149
	24	35.07	0.86	96.32	2.432	8.914	116.7	13.444
	25	38.06	1.30	102.169	3.589	9.791	125.017	15.097

[a] Model ages were calculated with the CRONUS-Earth online calculator, version 2.2 [*Balco et al.*, 2008] (available at http://hess.ess.washington.edu/math).

[b] Minimum model age, calculated with no erosion.

[c] Int. ±: internal (or analytical) uncertainty, which includes error from the blank and the AMS counting statistics.

[d] Ext. ±: external (or propagated) uncertainty, which takes into account uncertainty in the production rate and scaling factors.

[e] Maximum model age, calculated with a maximum erosion rate of 2.08 m/Ma.

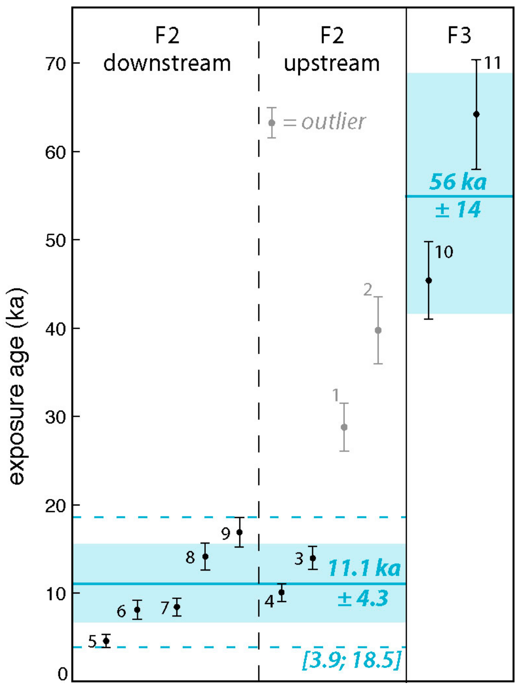

Figure 14. ^{10}Be cosmogenic radionuclide (CRN) model ages at the Jabal Al-Muhtadi site. Lines and colored bars represent the weighted mean ± standard deviation σ, based on ages represented in black. Ages in gray are visually defined outliers (see text).

3.2. ^{10}Be Cosmogenic Radionuclide Model Ages and Interpretation

3.2.1. The Jabal Al-Muhtadi Site

[39] We collected samples on surfaces F2 and F3, at locations shown in Figure 5. To date the offset alluvial fan F2, we sampled 9 granitic cobbles at the surface on either side of the fault. Care was taken to collect only well-embedded cobbles in the best-defined parts of surface F2, characterized by a darker color (Figure 13). Indeed, because of the small difference in height (~40 cm) between F2 and F1 (Figure 4b), we cannot totally rule out occasional contamination of surface F2 with younger cobbles during extreme flood events when F1 was still the active surface. Surface F3 is paved by 1 to 10 cm varnished pebbles and exhibits no cobbles. Two amalgamates of granitic and quartz vein pebbles were collected on a preserved part of surface F3, away from any regressive gully.

[40] The catchment area of the Wadi Al-Muhtadi is fairly large, about 32 km^2, with a length of 9 km. Yet the drainages are rather straight, taking advantage of preexisting fractures within the bedrock (Figure 2), limiting the possibilities for clasts to be temporarily stored in the wadis and, hence, to acquire inheritance related to transport duration. Inheritance related to preexposure prior to transport remains possible.

[41] ^{10}Be CRN model ages are reported in Tables 2a, 2b, and 2c and Figure 14. The two samples of amalgamated pebbles collected on surface F3 yield a mean age of 56 ± 14 ka for this surface. This age is consistent with that of 62 ± 5 ka determined by *Porat et al.* [2010] for an alluvial surface located 15 km to the south (Figure 1b), which is at the same relative level above the present-day channels as F3.

[42] On surface F2, west of the fault, four samples have CRN model ages ranging between 8.1 ± 1.0 and 16.9 ± 1.6 ka and one sample (4.6 ± 0.7 ka, no. 5) is significantly younger. East of the fault, two of the ages are 10.3 ± 1.0 and 14.1 ± 1.5 ka, comparable to the age population downstream, while the other two samples are much older (30 ± 3 ka, no. 1; 41 ± 4 ka, no. 2). The ages of those samples suggest that they

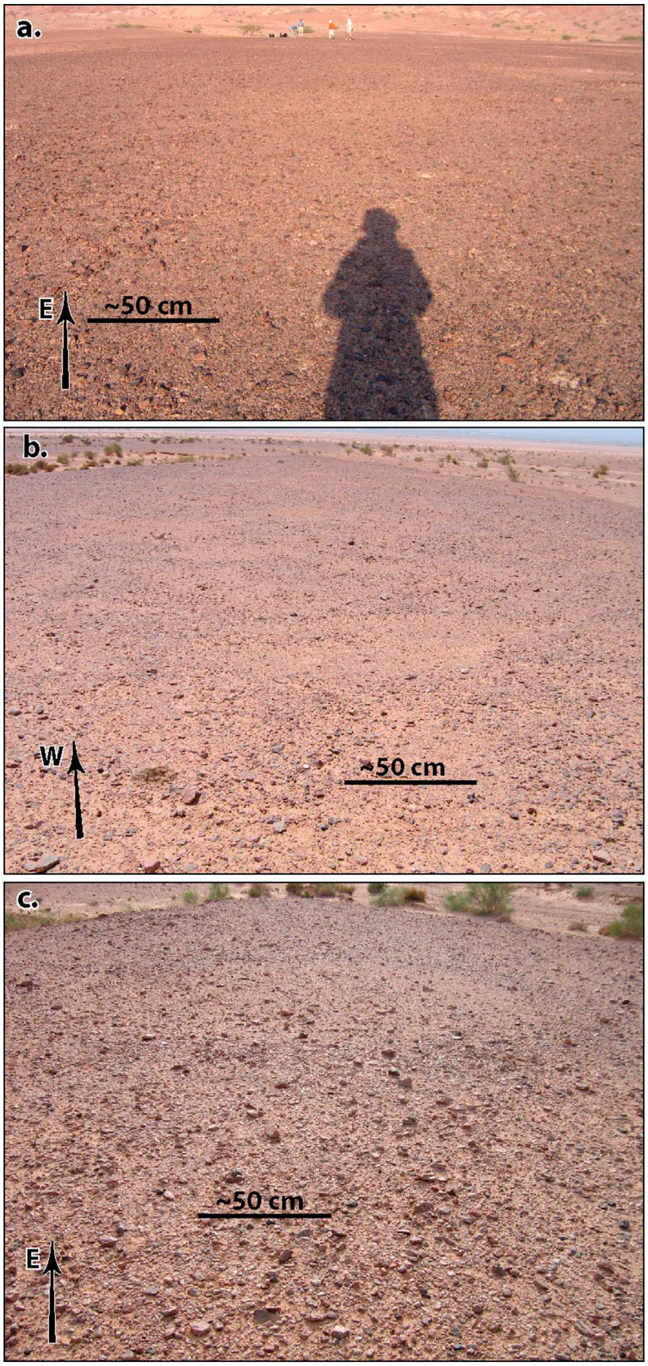

Figure 15. Sampling at the Hamrat Al-Fidan site. (a) View of surface F4W, south of channel C1′. The surface is dark and paved with pebbles. (b) View of surface F2W, which is lighter than F4 due to the less developed desert pavement and varnish. (c) View of surface F2E, which appears similar to F2W (Figure 15b).

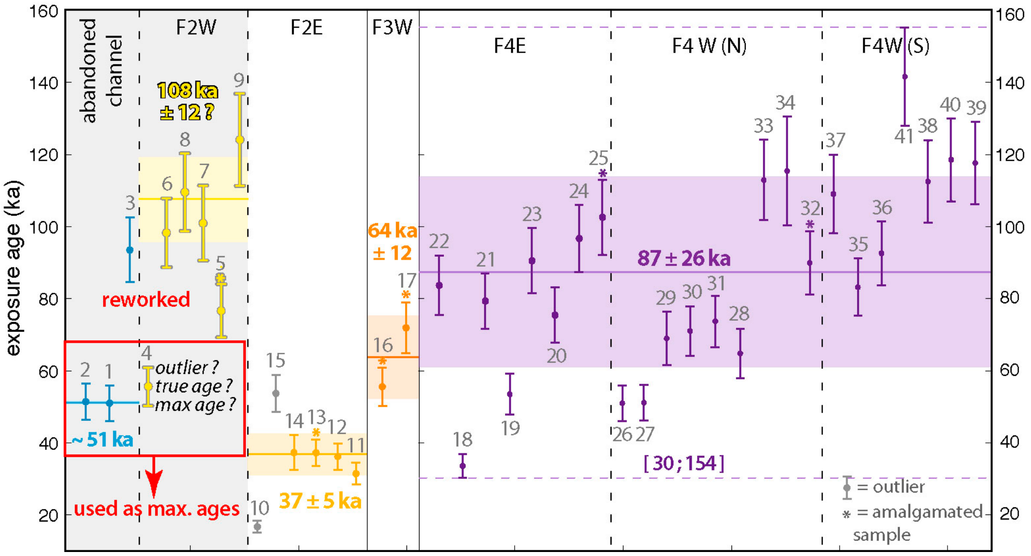

Figure 16. ^{10}Be CRN model ages at the Hamrat Al-Fidan site. Lines and colored bars represent the weighted mean ± standard deviation σ, based on selected ages. For surface F4, dotted lines limit the interval covered by all the ages. Surface names are labeled east (E) or west (W), according to their location relative to the fault. Surfaces F4W(N) and F4W(S) correspond to F4 west of the fault, north and south of channel C1′, respectively.

have been redeposited from an older alluvial deposit, such as F3, which is actively incised by current channels. Discarding those two samples, we compute an average age for F2 of 11.1 ± 4.3 ka, based on seven samples. The interval mean ± σ does not overlap the youngest age from sample 5. Because of the small height difference between F2 and F1, it is likely that this cobble was brought onto F2 during an exceptional flood that occurred after the abandonment of F2. Neglecting this possibility would lead to consideration of the conservative interval [3.9 ka; 18.5 ka].

3.2.2. The Hamrat Al-Fidan Site

[43] At Hamrat Al-Fidan we targeted surfaces F4 and F2 and the abandoned channel C2′, for which we could measure offsets. Surface F3 was also dated to get a better understanding of the alluvium emplacement history at this site. Sample locations are shown in Figure 9, and CRN model ages are reported in Tables 2a, 2b, and 2c and Figure 16. To avoid any confusion, surface names are labeled "E" or "W," according to their location relative to the fault.

[44] Surface F4 was sampled east and west of the fault (Figure 9). Care was taken to sample only pristine surfaces, not affected by surficial erosion (Figure 15). Twenty-two granitic cobbles and two amalgamated samples of quartz pebbles led to a widespread age distribution. CRN model ages range from 33 ± 3 to 141 ± 13 ka (samples 18 and 41), most of them (19 of 24) lying between 65 ± 7 and 118 ± 11 ka, amalgamated samples included (Tables 2a, 2b, and 2c and Figure 16).

[45] Before defining CRN model age clusters further, we investigated which mechanism(s) could be at the origin of such important scattering and whether the average age would be representative of the true age. Hereafter we consider two scenarios in which the use of the average age would be misleading: first, scattered inheritance from 0 to ~50 ka and, second, continuous activity of the surface during ~50 ka. In the first case, only the youngest samples would be appropriate for estimating the age of the surface. In the second case the entire interval would have to be considered.

[46] Because catchments at this site are very small (<1 km^2), inheritance related to temporary storage in the catchments seems unlikely. However, between the catchment outlet and the sampling site, the gentle ~1 km long slope of the bajada could account for a slow transit area where the clasts may be preexposed to cosmic-ray flux. The bajada setting of the site would also support the possibility of extended activity of the surfaces. In addition, the small catchments may not feed the drainages with a sufficient amount of clasts to totally cover older deposits. Such processes can hardly be quantified from our data and they have also probably evolved in parallel with climatic variations. The formation of four alluvial terrace levels within ~90 ka, however, suggests that surface activity is shorter than ~50 ka. Preexposure as large as ~50 ka is not supported by the age distribution obtained for F2E (Figure 16).

[47] Owing to the obvious complex mechanisms responsible for scattering, we proposed two levels of interpretation of these ages. First, we used all 24 ages, including their uncertainty, and we provided a conservative range of ages of [30 ka; 154 ka]. Then, from all the ages, we computed an average age of 87 ± 26 ka, which covers 17 of the 24 ages. Defining the age of surface F4 based only on the age distribution is not straightforward. Yet our morphostratigraphic analysis and the ages obtained for the other surfaces provide additional information. Sample 18 has an age similar to that of surface F2E; samples 19, 26, and 27 are slightly younger than F3W (Figure 16). Integrating these samples is inconsistent with our morphostratigraphic mapping. Hence, these younger samples may have been brought onto F4 during some more recent flood events, possibly related to the

emplacement of F3 and F2. Thus, we favor the average age of 87 ± 26 ka for surface F4.

[48] A difference in the age distribution on F4W, north and south of C1′, is worth noting. Samples 28 to 31 collected on F4W(N) exhibit slightly younger CRN model ages than the youngest sample collected on F4W(S) (n°35). This suggests that the active drainage system could have migrated from south to north, leaving the southern part inactive before the bajada was totally abandoned and later incised. This would be consistent with left-lateral offset of the western block relative to the feeding catchments.

[49] On surface F3, west of the fault (F3W), we could not find any cobbles. We collected amalgamated samples of quartz pebbles from two distinct parts of the surface (Figure 9). We obtained model ages of 72 ± 7 ka (no. 17) to the south and 55 ± 5 ka (no. 16) to the north (Table 2 and Figure 16). Averaging ages, we obtain 63 ± 12 ka for F3. Given the limited data for this surface and the fact that we used amalgamated samples, these results should be interpreted with care. However, they would mean that the southern lobe was deposited before the northern one, in keeping with the motion on the fault.

[50] On the fan F2W, inset in the northern part of F3W (Figure 9), we collected five cobbles and one amalgamated sample of granitic pebbles. Four cobbles display CRN model ages between 98 and 124 ka and one is significantly younger, at 55 ± 5 ka (no. 4). The amalgamated sample (no. 5), which lies in between, at 76 ± 7 ka, reflects the scattering of the CRN model ages on this surface. We also investigated the abandoned channel C2′ incised into F2W (Figure 9). The stream bed of C2′ has probably been preserved since it was disconnected from C1, as it passed in front of only one minor drainage, the gully S1. Narrow and winding, S1 is probably not powerful enough to have significantly modified the stream bed of C2′, either by significant incision or by influx of clastic material. Care was taken to collect well-rooted cobbles from the best-preserved areas, avoiding the shallow rill incised in the stream bed and the colluvial material present along the drainage banks. One cobble yields a model age of 93 ± 9 ka (no. 3) and two (nos. 1 and 2) provide significantly younger ages, 51 ± 5 ka.

[51] The CRN model ages from both F2W and C2′ appear to be much older than expected from the surface appearance of F2W (limited desert varnish and pavement) and from its morphologic position relative to F3 and F4. Actually, the general age distribution of F2W, in addition to sample 3 from C2′, is rather similar to the age distribution of F4. The youngest model age of F2W (55 ± 5 ka, sample 4) is similar to the model age of sample 16 (55 ± 5 ka), collected on the northern lobe of F3W. The 51 ka ages of channel C2′ are accordingly slightly younger than the youngest sample of F2W. We interpret these ages, or at least the older ones, as reworked material from F4 and, possibly, F3 types of alluvium. This idea is supported by the incision within F4E upstream of F2W and the required remobilization of F3W prior to the emplacement of F2W. Regarding the youngest ages (no. 4 on F2W and nos. 1 and 2 within C2′), either they correspond to the true ages of F2W and C2′ or they have also been redeposited, in which case they would represent a maximum age.

[52] Further information may be obtained by examining the data from F2E, east of the fault, where we collected five cobbles and one amalgamated sample of granitic pebbles (Figure 9). Figures 15b and 15c illustrate the similarity between the two surfaces F2, east and west of the fault: they are light in color, with few cobbles and little sand between pebbles. Four of the ages (including that of the amalgamated sample) range between 31 ± 3 ka and 42 ± 5 ka; one is much younger (17 ± 2 ka, no. 10) and one is significantly older (54 ± 5 ka, no. 15). Discarding samples 10 and 15, we obtain an average age of 37 ± 5 ka based on four samples. If this surface truly correlates with F2W, as supported by their comparable appearance and similar relative height above the active channels, these ages attest that the samples of F2W are reworked from older deposits. This would also confirm surface F4E to be a source of material for F2W, as F2E, located upstream from that source, has not been contaminated.

4. Slip Rate on the Fault

[53] The slip rate on the fault is obtained by dividing the cumulative lateral offset by the age of the offset feature. The type of exposure age to be considered depends on the nature of the marker used to determine the offset. In our study we match both alluvial fans and channels. When the shape of a fan is restored, the average exposure age should be used. When the marker is a channel incised in a specific terrace, one should refer to the timing of surface incision, usually estimated by the abandonment age of the incised surface (i.e., a maximum age), assuming that incision shortly follows abandonment.

[54] To compute fault slip rates we divided the lower-bound offset by the oldest age value and the upper-bound offset by the youngest age value. We then obtained the minimum and maximum fault slip rates, from which we calculated the mean and associated uncertainty.

4.1. Slip Rate Derived From the Jabal Al-Muhtadi Offset Alluvial Fans

[55] At Jabal Al-Muhtadi an offset of 48 ± 7 m was determined for surface F2 (Figure 6), in which configuration the alluvial fan is restored to its initial geometry. Combining this offset with an average age of 11.1 ± 4.3 ka for this surface yields a slip rate of 5.4 ± 2.7 mm/a. The minimum and maximum offsets of 24 and 64 m, which we argued to be strictly under- and overestimated, together with the conservative age interval of [3.9 ka; 18.5 ka], yield slip rate bounds of 1.3 and 16.4 mm/a.

[56] Owing to the scarce data for surface F3 at Jabal Al-Muhtadi west of the fault, we could propose only four ranges of possible offsets, the smallest two being the most likely (255 ± 8 and 370 ± 18 m; Figure 7). Using these offsets and the average age of F3 (56 ± 14 ka), we obtain slip rate ranges of 3.5–6.3 and 5.0–9.2 mm/a, respectively. These values, especially the first one, are in agreement with the Early Holocene slip rate determined at the same site. Larger offsets would yield the significantly faster slip rates of 7.1–14.8 and 9.4–16.7 mm/a.

4.2. Late Pleistocene Slip Rate Derived From the Hamrat Al-Fidan Site

[57] At the Hamrat Al-Fidan site we could determine two different offsets, for surface F2 and the abandoned channel

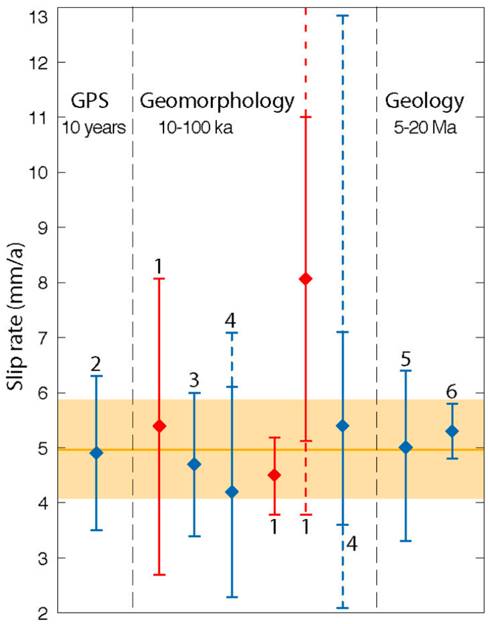

Figure 17. Selected slip rates along the Wadi Araba segment of the Dead Sea fault. (1) This study; (2) *Le Beon et al.* [2008]; (3) *Niemi et al.* [2001]; (4) *Klinger et al.* [2000a]; (5, 6) various studies based on geological offsets and fault structure (see text). Dotted lines represent less likely values. Slip rates from these studies yield a mean slip rate of 5.1 ± 0.9 mm/a.

C2′ incised within F2W and for surface F4 (Figures 9, 11, and 12). The offset of surface F2 and of the abandoned channel C2′ is 160 ± 8 m (Figure 11). As detailed in section 3.2.2, we interpreted the samples collected on F2 west of the fault and in the channel as being reworked from older deposits. Nevertheless, the youngest ages, if interpreted as maximum ages, may be used to determine the minimum slip rate. Using maximum ages of 55 ± 5 ka (sample 4) for F2W and of 51 ± 5 ka (samples 1 and 2) for C2′ (Tables 2a, 2b, and 2c), we obtain minimum slip rates of 2.9 ± 0.5 and 3.2 ± 0.5 mm/a, respectively. Because the surface has been incised before being offset (see section 2.2.2), dating from the channel provides the best constraint. Provided appropriate surface correlation across the fault, we propose to use the exposure age of F2E (37 ± 5 ka) to determine the minimum fault slip rate. We obtain 4.5 ± 0.9 mm/a. Because incision shortly followed surface abandonment, the upper part of this interval is probably a closer estimate of the fault slip rate.

[58] For surface F4, adjustment of channels C1 and C1′ on both sides of the fault leads to an offset of 626 ± 37 m (Figure 12), also consistent with the shape of surface F4. As detailed in section 3.2.2, we favor an average exposure age of 87 ± 26 ka. Combining the 626 ± 37 m offset with this age, we obtain a slip rate of 8.1 ± 2.9 mm/a. Using the interval of [30 ka; 154 ka] yields a conservative range of 3.8–22.1 mm/a, which accounts for any depositional scenario for F4 itself. Yet the upper values are not consistent with the chronology of surface emplacement at the scale of the site. Because the offset marker refers to an incision event that occurred after the abandonment of F4, this value is a minimum. Competition between uplift and incision, especially east of the fault, and appropriate reconstruction of the shape of F4 strongly suggest that incision shortly followed abandonment of the surface. We provide a conservative upper bound for the slip rate using the maximum offset of 737 m (Figure 12c), obtained by realigning the southern risers of F4 and which we argue to be overestimated. We obtain 9.3 ± 2.8 mm/a from the average age of 87 ± 26 ka and slip rate bounds of 4.8 and 24.6 mm/a when we consider the interval [30 ka; 154 ka].

5. Discussion and Conclusions

5.1. Comparison With Previous Slip Rates on the Wadi Araba Fault Segment

[59] Numerous studies have investigated the slip rate on the WAF using various tools, such as spatial geodesy, geomorphology, and geology (Figure 17). All studies mentioned hereafter focus on the same fault segment, allowing direct comparison.

[60] On the short time scale of a few years, studies investigated the present-day slip rate of the southern DSF based on GPS measurements. Earliest estimates used continuous data from the Israeli permanent network [*Pe'eri et al.*, 2002; *Wdowinski et al.*, 2004], which has the weakness of being located mostly on one side of the fault. The best estimate on the WAF is 2.9 ± 1.1 mm/a [*Wdowinski et al.*, 2004]. This result has been improved recently from a denser GPS campaign-style network distributed on both sides of the WAF [*Le Béon et al.*, 2008]. This work yielded a slip rate of 4.9 ± 1.4 mm/a over a 6 year time period, in agreement with regional block models [*Reilinger et al.*, 2006].

[61] The Early Holocene slip rate of WAF has been investigated independently in two studies based on the same site in the northern Wadi Araba (Figure 1b), where three successive alluvial surfaces and gullies are offset by the fault. *Klinger et al.* [2000a] and *Niemi et al.* [2001] provide a slip rate of 3.4–6.1 mm/a since ~15 ka. The slip rate of 5.4 ± 2.7 mm/a, which we determined over ~11 ka in the southern Wadi Araba at the Jabal Al-Muhtadi site, is in very good agreement with these results. Previous studies at Jabal Al-Muhtadi led to offsets of 540–600 m [*Zak and Freund*, 1966; *Galli*, 1999], much larger than those proposed here. These studies unfortunately lacked proper dating and our new data set shows that the alluvial surfaces matched to each other are actually characterized by different ages.

[62] In the northern Wadi Araba, *Klinger et al.* [2000a] investigated a Late Pleistocene alluvial fan (Figure 1b), dated between 70 ka and 140 ka using ^{10}Be CRN model ages of chert cobbles and U-series of overlying Lake Lisan deposits [*Klinger et al.*, 2003]. Restoration of the fan to the mouth of the feeding channel provides an offset of 300 to 900 m, with a best value of 500 m. The resulting slip rates range from 2.1 to 12.9 mm/a, with a best interval of 3.6–7.1 mm/a. At a comparable time scale (87 ± 26 ka), our study provides a wide conservative interval of slip rates, from 4.2 to 20.1 mm/a, with preferred values of 5.2–10.9 mm/a. The union of best intervals proposed by both studies suggests that slip rates of 5 to 8 mm/a are more likely.

[63] At longer time scales *Ginat et al.* [1998] obtained a slip rate of 3–7.5 mm/a since the Pliocene, based on the

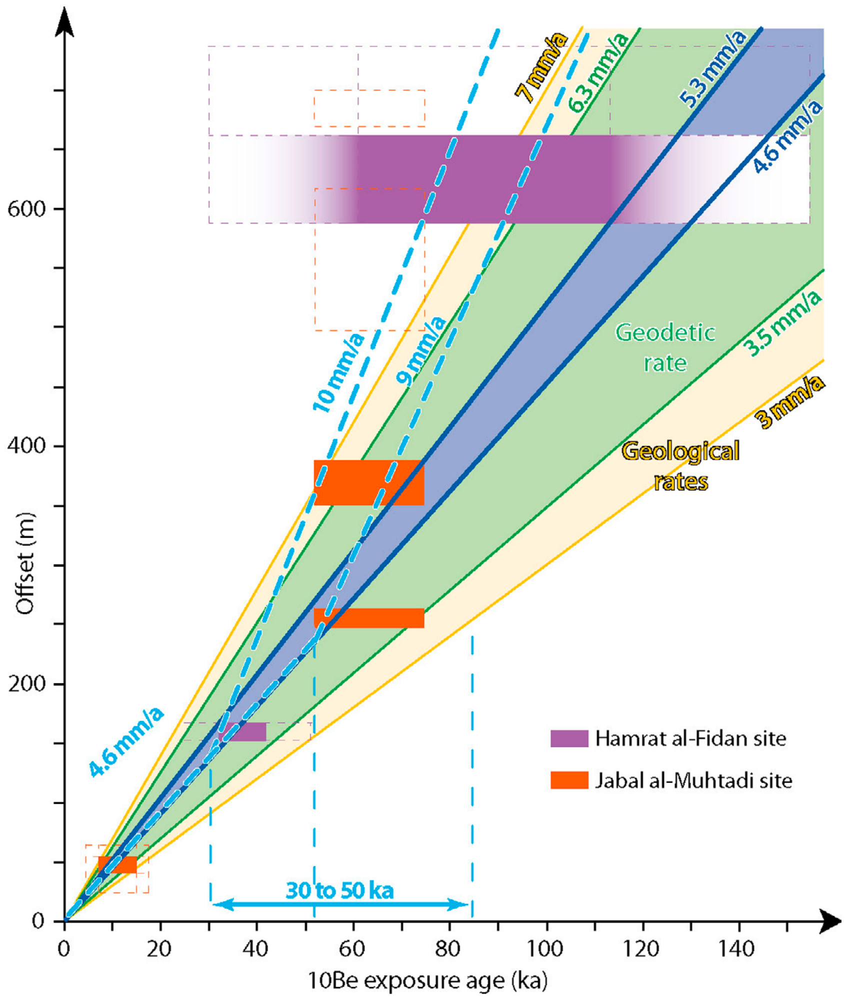

Figure 18. Possible scenarios of slip rate evolution over time based on offset and age constraints determined in this study. Colored rectangles show the best age and offset constraints. The constraints that we judged to be less likely are represented by dotted lines. Dark blue dotted trend lines represent lower and upper bounds for the fault slip rate (>3.2 mm/a and <12.7 mm/a, respectively). Dark blue shaded area corresponds to a constant slip rate. Light blue dashed lines show examples of two possible scenarios of varying slip rate over time (see text). Yellow and green shaded areas represent and geodetic slip rates, respectively.

offset conglomerate of a paleoriver that ran across the Wadi Araba and on the offset of undated large alluvial fans within the Wadi Araba. *Garfunkel* [1981] proposed a cumulative offset of 35–40 km, later reevaluated at 30 km [*Garfunkel and Ben-Avraham*, 2001], by closing the pull-apart structures of the Dead Sea basin and of the Gulf of Aqaba. Assuming an Early Pliocene age for the Dead Sea basin [*Garfunkel and Horowitz*, 1966], this reconstruction leads to a slip rate of 6 mm/a since the last 5 Ma. *Freund et al.* [1968, 1970] reported a 40–45 km offset of numerous Miocene geological formations (7–12 Ma), which yields a slip rate of 3.3–6.4 mm/a. At longer time scales, a cumulative offset of 105 km, recorded by Precambrian to Late Cretaceous rocks [*Dubertret*, 1932; *Quennell*, 1959; *Freund et al.*, 1968, 1970], is generally accepted on the DSF. Yet the timing of the initiation of the left-lateral shear remains debated. Values of 18–22 Ma have been proposed based on extensive basaltic dykes along the Gulf of Aqaba [e.g., *Bartov et al.*, 1980]. This would lead to an average slip rate of 5.3 ± 0.5 mm/a.

5.2. Slip Rate Evolution Through Time on the Wadi Araba Fault Segment

[64] The sites presented in this study provide slip rates averaged over three time scales: ~11, ~37, and ~87 ka. Previous studies along the same fault segment of the Dead Sea Fault provide slip rates at time scales ranging from a few years to several millions of years (Figure 17), offering the possibility to look at fault slip rate evolution through time.

[65] Good agreement is found among the geodetic slip rate, the Early Holocene slip rate, and the post-Oligocene slip rate along the WAF. The different techniques converge to an average rate of 5.1 ± 0.9 mm/a (Figure 17). Despite larger uncertainties, the best intervals proposed for the Late Pleistocene slip rate also overlap this value. Figure 18

summarizes the Early Holocene and Late Pleistocene data presented in this study. Our data set may be fit with a straight line, the slope of which corresponds to a constant slip rate of 4.6–5.3 mm/a (Figure 18), similar to the GPS and geologic slip rates. However, due to the large uncertainty in the age of the Late Pleistocene geomorphic marker, scenarios that include temporal variations in fault slip rate are also possible. In Figure 18 we propose two alternative examples; any and all intermediate possibilities would be valid as well. They show variations by a factor of 2 at the fairly long time scales of ~30 to ~50 ka, which would represent 30 to 50 earthquake cycles, considering the average recurrence interval of large earthquakes observed on the northern DSF during the Holocene [*Meghraoui et al.*, 2003; *Daëron et al.*, 2005, 2007]. To summarize, we lack resolution to fully resolve the question of temporal variations versus consistency of the fault slip rate of the WAF. Overall, the geodetic slip rate and slip rates at longer time scales are not inconsistent with each other, given the uncertainties, which is not the case for all major strike-slip faults (e.g., the Altyn Tagh Fault in Tibet [*Bendick et al.*, 2000; *Mériaux et al.*, 2004, 2005; *Wright et al.*, 2004; *Peltzer et al.*, 2006; *Jolivet et al.*, 2008]). Millennial-scale variations cannot be addressed owing to the shortest time window of ~11 ka of our study.

[66] The temporal distribution of large earthquakes on the Dead Sea Fault may be used as a proxy of the slip rate evolution over time. *Hamiel et al.* [2009] concluded a constant fault slip rate based on historical seismicity and paleoseismological data from indirect records and observations from secondary tectonic features, however. An exceptional paleoseismic record exists within the Late Pleistocene Lisan Lacustrine Formation in the southern Dead Sea basin [*Marco et al.*, 1996; *Marco and Agnon*, 2005; *Agnon et al.*, 2006; *Begin et al.*, 2005]. During the period 15–70 ka, the distribution of breccia layers related to local $M \geq 5.5$ earthquakes and of peculiar seismites related to local $M > 7$ earthquakes revealed periods of earthquake clustering of ~10 ka followed by periods of relative quiescence of similar duration; a cluster of nine earthquakes occurred between 50 and 55 ka. However, interpreting this record as slip rate variations on a particular fault is not straightforward. First, the source of these events cannot be identified: any segments from Lebanon to the Gulf of Aqaba are candidates. Second, $M5.5$–$M6$ earthquakes are certainly too small to produce large displacement on the fault plane and contribute significantly to the slip rate.

[67] Along the nearby fault segment of the Jordan Valley Fault (Figure 1a), north of the Dead Sea, *Ferry et al.* [2007] observed millennial-scale variations in fault slip rate during the Late Pleistocene. They report slip rate variations from 3.5 to 11.0 mm/a at the time scale of 2 ka during the Holocene, which are smoothed when a time window of 4 ka is considered, varying from ~3.5 to ~6 mm/a. The average slip rate of ~4.9 mm/a since 48 ka is in good agreement with the results obtained south of the Dead Sea. Millennial-scale slip rate variations are also suggested along the northern DSF in Syria [*Meghraoui et al.*, 2003]. On the basis of three earthquakes that occurred during the last 2 ka, the authors report a slip rate of 6.9 ± 0.1 mm/a, which is significantly higher than the GPS slip rate along the same fault segment (1.8–3.3 mm/a [*Alchalbi et al.* [2010]) and the Holocene slip rates observed along the southern DSF.

[68] *Weldon et al.* [2004] also reported secular slip rate variations by a factor of 3 along the San Andreas Fault, in relation to earthquake clustering at a time scale of 200 years. These variations involve only a few earthquake cycles. Larger-scale (≥10 ka) variations in fault slip rate have rarely been reported on large strike-slip faults, with the exception of 10–100 ka variations observed along the San Andreas Fault system since 1.5 Ma in the specific case of subparallel fault branches [*Bennett et al.*, 2004], along which activity could switch from one fault to the other. The Karakorum Fault, in Tibet, or the North Anatolian Fault, for example, show fairly constant slip rates at time scales of 1 ka to several million years [*Chevalier et al.*, 2005; *Kozaci et al.*, 2009]. Regarding the WAF, complex fault interactions can be ruled out due to its single-strand geometry. Hence, within the limitation of the uncertainties currently available for the different studies, including this work, it seems more likely that the slip rate is fairly constant along the southern DSF over a period of at least 100 ka.

[69] **Acknowledgments.** We thank Jérôme Van der Woerd for fruitful discussion during this work and Anne-Claire Laurent-Morillon for digitalization of landscape interpretations. Thoughtful reviews by G. Hilley and an anonymous reviewer helped to improve the manuscript. Financial support was provided by the French INSU/CNRS programs DyETI and ACI-FNS "Aléas et changements globaux" and by the French Embassy in Jordan. This is IPGP contribution number 3045.

References

Agnon, A., C. Migowski, and S. Marco (2006), Intraclast breccias in laminated sequences reviewed: recorders of paleo-earthquakes, in *New frontiers in Dead Sea Paleoenvironmental Research: Geological Society of America Special Paper 401*, edited by Y. Enzel et al., pp. 195–214, doi:110.1130/2006.2401(1113).

Alchalbi, A., et al. (2010), Crustal deformation in northwestern Arabia from GPS measurements in Syria: Slow slip rate along the northern Dead Sea Fault, *Geophys. J. Int.*, 125–135, doi:110.1111/j.1365-1246X.2009.04431.x.

Balco, G., J. O. Stone, N. A. Lifton, and T. Dunai (2008), A complete and easily accessible means of calculating surface exposure ages or erosion rates from 10Be and 26Al measurements, *Quat. Geochronol.*, *3*, 174–195.

Bartov, Y., G. Steinitz, M. Eyal, and Y. Eyal (1980), Sinistral movement along the Gulf of Aqaba—its age and relation to the opening of the Red Sea, *Nature*, *285*, 220–222.

Begin, Z. B., D. M. Steinberg, G. A. Ichinose, and S. Marco (2005), A 40,000 year unchanging seismic regime in the Dead Sea rift, *Geology*, *33*(4), 257–260.

Bendick, R., R. Bilham, J. Freymueller, K. Larson, and G. Yin (2000), Geodetic evidence for a low slip rate in the Altyn Tagh fault system, *Nature*, *404*, 69–72.

Bennett, R. A., A. M. Friedrich, and K. P. Furlong (2004), Codependent histories of the San Andreas and San Jacinto fault zones from inversion of fault displacement rates, *Geology*, *32*(11), 961–964.

Briner, J. P., D. S. Kaufman, W. F. Manley, R. C. Finkel, and M. W. Caffee (2005), Cosmogenic exposure dating of the late Pleistocene moraine stabilisation in Alaska, *Geol. Soc. Am. Bull.*, *117*, 1108–1120, doi:1110.1130/B25649.25641.

Bull, W. B. (1991), *Geomorphic Responses to Climatic Change*, Oxford University Press, New York.

Chevalier, M. L., F. J. Ryerson, P. Tapponnier, R. C. Finkel, J. van der Woerd, H. B. Li, and Q. Liu (2005), Slip-rate measurements on the Karakorum Fault may imply secular variations in fault motion, *Science*, *307*, 411–414.

Daëron, M., L. Benedetti, P. Tapponnier, A. Sursock, and R. Finkel (2004), Constraints on the post ~25-ka slip rate of the Yammouneh fault (Lebanon) using in-situ cosmogenic Cl^{36} dating of offset limestone-clast fans, *Earth Planet. Sci. Lett.*, *227*, 105–119.

Daëron, M., Y. Klinger, P. Tapponnier, A. Elias, E. Jacques, and A. Sursock (2005), Sources of the large AD1202 and 1759 Near East earthquakes, *Geology*, *53*(7), 529–532.

Daëron, M., Y. Klinger, P. Tapponnier, A. Elias, E. Jacques, and A. Sursock (2007), 12,000-year-long record of 10 to 13 paleo-earthquakes on the Yammoûneh fault (Levant fault system, Lebanon), *Bull. Seism. Soc. Am.*, *97*(3), 749–771.

Davis, J. C., I. D. Proctor, J. R. Southon, M. W. Caffee, D. W. Heikkinen, M. L. Roberts, K. W. Turteltaub, D. E. Nelson, D. H. Loyd, and J. S. Vogel (1990), LLNL/UC AMS facility and research program, *Nucl. Instrum. Methods Phys. Res. Sect. B*, *52*, 269–272.

Dubertret, L. (1932), Les formes structurales de la Syrie et de la Palestine, *C.R. Acad. Sci. Paris*, *195*, 65–67.

Elias, A., et al. (2007), Active thrusting offshore Mount Lebanon: source of the tsunamigenic A.D. 551 Beirut-Tripoli earthquake, *Geology*, *35*, 755–758, doi:710.1130/G2363A.

Ferry, M., M. Meghraoui, N. Abou Karaki, M. Al-Taj, H. Amoush, S. Al-Dhaisat, and M. O. Barjous (2007), A 48-kyr-long slip rate history for the Jordan Valley segment of the Dead Sea Fault, *Earth Planet. Sci. Lett.*, *260*, 394–406.

Finkel, R. C., and M. Suter (1993), AMS in earth sciences: Technique and applications, *Adv. Anal. Geochem.*, *1*, 1–114.

Freund, R., I. Zak, and Z. Garfunkel (1968), Age and rate of the sinistral movement along the Dead Sea Rift, *Nature*, *220*, 527–538.

Freund, R., Z. Garfunkel, I. Zak, M. Goldberg, T. Weisbrod, and B. Derin (1970), The shear along the Dead Sea rift, *Philos. Trans. R. Soc. A*, *267*, 107–130.

Galli, P. (1999), Active tectonics along the Wadi Araba-Jordan Valley transform fault, *J. Geophys. Res.*, *104*, 2777–2796.

Garfunkel, Z. (1981), Internal structure of the Dead Sea Leaky Transform (rift) in relation to plate kinematics, *Tectonophysics*, *80*, 81–108.

Garfunkel, Z., and Z. Ben-Avraham (2001), Basins along the Dead Sea Transform, in *Peri-Tethys Memoir 6: Peri-Tethyan Rift/Wrench Basins and Passive Margins*, *Mém. Mus. Natl. Hist. Nat.*, 186, edited by W. C. P. A. Ziegler, A. H. F. Robertson, and S. Crasquin-Soleau, pp. 607–627, Mus. Natl. Hist. Nat., Paris, ISBN: 2-85653-528-3.

Garfunkel, Z., and A. Horowitz (1966), The Upper Tertiary and Quaternary morphology of the Negev, Israel, *Isr. J. Earth Sci.*, *15*, 101–117.

Ginat, H., T. Enzel, and Y. Avni (1998), Translocated Plio-Pleistocene drainage systems along the Arava fault of the Dead Sea Transform, *Tectonophysics*, *284*, 151–160.

Gosse, J. C., and F. M. Phillips (2001), Terrestrial in situ cosmogenic nuclides: Theory and application, *Quat. Sci. Rev.*, *20*, 1475–1560.

Hamiel, Y., R. Amit, Z. B. Begin, S. Marco, O. Katz, A. Salamon, E. Zilberman, and N. Porat (2009), The Seismicity along the Dead Sea Fault during the last 60,000 years, *Bull. Seismol. Soc. Am.*, *99*, 2020–2026, doi:2010.1785/0120080218.

Hetzel, R., S. Niedermann, S. Ivy-Ochs, P. W. Kubik, M. Tao, and B. Gao (2002), ^{21}Ne versus ^{10}Be and ^{26}Al exposure ages of fluvial terraces: The influence of crustal Ne in quartz, *Earth Planet. Sci. Lett.*, *201*(3–4), 575–591.

Jolivet, R., R. Cattin, N. Chamot-Rooke, C. Lasserre, and G. Peltzer (2008), Thin-plate modeling of interseismic deformation and asymetry across the Altyn Tagh fault zone, *Geophys. Res. Lett.*, *35*, L02309, doi:10.1029/2007GL031511.

Klinger, Y., J. P. Avouac, N. Abou Karaki, L. Dorbath, D. Bourles, and J. L. Reyss (2000a), Slip rate on the Dead Sea Transform Fault in northern Araba Valley (Jordan), *Geophys. J. Int.*, *142*, 755–768.

Klinger, Y., J. P. Avouac, L. Dorbath, N. Abou Karaki, and N. Tisnerat (2000b), Seismic behaviour of the Dead Sea Fault along Araba Valley, Jordan, *Geophys. J. Int.*, *142*, 769–782.

Klinger, Y., J.-P. Avouac, D. Bourles, and N. Tisnerat (2003), Alluvial deposition and lake-level fluctuations forced by Late Quaternary climate change: The Dead Sea case example, *Sediment. Geol.*, *162*, 119–139.

Kohl, C. P., and K. Nishiizumi (1992), Chemical isolation of quartz for measurement of in situ-produced cosmogenic nuclides, *Geochim. Cosmochim. Acta*, *56*, 3583–3587.

Kozaci, Ö., J. F. Dolan, and R. C. Finkel (2009), A late Holocene slip rate for the central North Anatolian fault, at Tahtaköprü, Turkey, from cosmogenic 10Be geochronology: Implications for fault loading and strain release rates, *J. Geophys. Res.*, *114*, B01405, doi:10.1029/2008JB005760.

Lal, D. (1991), Cosmic ray labeling of erosion surfaces: In situ production rates and erosion models, *Earth Planet. Sci. Lett.*, *104*, 424–439.

Le Béon, M. (2008), Cinématique d'un segment de faille décrochante à différentes échelles de temps: La faille du Wadi Araba, segment sud de la faille transformante du Levant, Ph.D. thesis (in English), 304 pp., Institut de Physique du Globe, Paris.

Le Béon, M., Y. Klinger, A.-Q. Amrat, A. Agnon, L. Dorbath, G. Baer, J.-C. Ruegg, O. Charade, and O. Mayyas (2008), Slip rate and locking-depth from GPS profiles across the southern Dead Sea Transform, *J. Geophys. Res.*, *113*, B11403, doi:10.1029/2007JB005280.

Marco, S., and A. Agnon (2005), High-resolution stratigraphy reveals repeated earthquake faulting in the Masada Fault Zone, Dead Sea Transform, *Tectonophysics*, *408*, 101–112.

Marco, S., M. Stein, A. Agnon, and H. Ron (1996), Long-term earthquake clustering: A 50,000-year paleoseismic record in the Dead Sea Graben, *J. Geophys. Res.*, *101*, 6179–6191.

Marco, S., T. Rockwell, A. Heimann, and U. Frieslander (2005), Late Holocene activity of the Dead Sea transform revealed in 3D paleoseismic trenches on the Jordan Gorge segment, *Earth Planet. Sci. Lett.*, *234*, 189–205.

Matmon, A., O. Simhai, R. Amit, I. Haviv, N. Porat, E. McDonald, L. Benedetti, and R. Finkel (2009), Desert pavement-coated surfaces in extreme deserts present the longest-lived landforms on Earth, *Geol. Soc. Am. Bull.*, *121*, 688–697, doi:610.1130/B26422.26421.

Meghraoui, M., et al. (2003), Evidence for 830 years of seismic quiescence from palaeoseismology, archaeoseismology and historical seismicity along the Dead Sea Fault in Syria, *Earth Planet. Sci. Lett.*, *210*, 35–52.

Meyer, B., P. Tapponnier, L. Bourjot, F. Metivier, Y. Gaudemer, G. Peltzer, G. Shunmin, and C. Zhitai (1998), Crustal thickening in Gansu-Qinghai, litospherique mantle subduction, and oblique, strike-slip controlled growth of the Tibet plateau, *Geophys. J. Int.*, *135*, 1–47.

Mériaux, A.-S., F. J. Ryerson, P. Tapponnier, J. Van der Woerd, R. C. Finkel, X. Xu, Z. Xu, and M. W. Caffee (2004), Rapid slip along the central Altyn Tagh Fault: Morphochronologic evidence from Cherchen He and Sulamu Tagh, *J. Geophys. Res.*, *109*, B06401, doi:10.1029/2003JB002558.

Mériaux, A.-S., K. Sieh, R. C. Finkel, C. M. Rubin, M. H. Taylor, A. J. Meltzner, and F. J. Ryerson (2009), Kinematic behavior of southern Alaska constrained by westward decreasing postglacial slip rates on the Denali Fault, Alaska, *J. Geophys. Res.*, *114*, B03404, doi:10.1029/2007JB005053.

Mériaux, A.-S., et al. (2005), The Aksay segment of the northern Altyn Tagh fault: Tectonic geomorphology, landscape evolution, and Holocene slip rate, *J. Geophys. Res.*, *110*, B04404, doi:10.1029/2004JB003210.

Niemi, T. M., H. W. Zhang, M. Atallah, and J. B. J. Harrison (2001), Late Pleistocene and Holocene slip rate of the northern Wadi Araba fault, Dead Sea Transform, Jordan, *J. Seismol.*, *5*, 449–474.

Nishiizumi, K., M. Imamura, M. W. Caffee, J. R. Southon, R. C. Finkel, and J. McAninch (2007), Absolute calibration of 10Be AMS standards, *Nucl. Instrum. Methods Phys. Res. Sect. B*, *258*, 403–413.

Pe'eri, S., S. Wdowinski, A. Shtibelman, N. Bechor, Y. Bock, R. Nikolaidis, and M. van Domselaar (2002), Current plate motion across the Dead Sea Fault from three years of continuous GPS monitoring, *Geophys. Res. Lett.*, *29*(14), 1697, doi:10.1029/2001GL013879.

Peltzer, G., A. Socquet, C. Lasserre, A. Meriaux, P. Tapponnier, and R. Ryerson (2006), InSAR observations of interseismic strain along the central Altyn Tagh fault consistent with Holocene slip rate, *Eos Trans. AGU*, *87*(52), Fall Meet. Suppl., Abstract T21E-02.

Porat, N., R. Amit, Y. Enzel, E. Zilberman, Y. Avni, H. Ginat, and D. Gluck (2010), Abandonment ages of alluvial landforms in the hyper-arid Negev determined by luminescence, *J. Arid. Environ.*, *74*, 861–869, doi:810.1016/j.jaridenv.2009.1010.1018.

Quade, J. (2001), Desert pavements and associated rock varnish in the Mojave Desert: How old can they be? *Geology*, *29*(9), 855–858.

Quennell, A. M. (1958), The structural and geomorphic evolution of the Dead Sea Rift, *Q. J. Geol. S. London*, *114*, 1–24.

Quennell, A. (1959), Tectonics of the Dead Sea rift, paper presented at Int. Geol. Congr. Mex., XX Session, pp. 385–405.

Rabb'a, I. (1994), The geology of the Al-Qurayqira (Jabal Hamra Faddan), Map sheet no. 3051 II, Natural Resources Authority of the Hashemite Kingdom of Jordan, Amman.

Rashdan, M. (1987), Geological of Wadi Araba and Al-Aqaba area, Map sheet nos. 2949-II and 3049-III, 1:50;000, Natural Resources Authority of the Hashemite Kingdom of Jordan, Amman.

Regard, V., O. Bellier, R. Braucher, F. Gasse, D. Bourlès, J. Mercier, J.-C. Thomas, M. R. Abbassi, E. Shabanian, and S. Soleymani (2006), 10Be dating of alluvial deposits from southeastern Iran (the Hormoz Strait area), *Palaeogeogr., Palaeoclimatol. Palaeoecol.*, *242*, 36–53.

Reilinger, R., et al. (2006), GPS constraints on continental deformation in the Africa-Arabia-Eurasia continental collision zone and implications for the dynamics of plate interactions, *J. Geophys. Res.*, *111*, B05411, doi:10.1029/2005JB004051.

Ritz, J.-F., R. Vassallo, R. Braucher, E. T. Brown, S. Carretier, and D. Bourles (2006), Using in situ-produced 10Be to quantify active tectonics in the Gurvan Bogd mountain range (Gobi-Altay, Mongolia), *Geol. Soc. Am. Spec. Pap.*, *415*, 87–110.

Ryerson, F. J., P. Tapponnier, R. C. Finkel, A.-S. Meriaux, J. Van Der Woerd, C. Lasserre, M.-L. Chevalier, X. Xu, H. Li, and G. C. P. King (2006), Applications of morphochronology to the active tectonics of Tibet, in *In Situ-Produced Cosmogenic Nuclides and Quantification of*

Geological Processes, Geological Society of America Special Papers, Issue 415, edited by L. L. Siame et al., pp. 61–86, GSA, Denver, Colo., doi:10.1130/2006.2415(1105).

Stone, J. O. (2000), Air pressure and cosmogenic isotope production, *J. Geophys. Res.*, *105*, 23,753–23,759.

Tapponnier, P., F. J. Ryerson, J. Van Der Woerd, A. S. Meriaux, and C. Lasserre (2001), Long-term slip rates and characteristic slip: keys to active fault behaviour and earthquake hazard, *C. R. Acad. Sci., Ser. IIa, Sci. Terre Planetes Paris*, *333*, 483–494.

Van der Woerd, J., F. J. Ryerson, P. Tapponnier, Y. Gaudemer, R. Finkel, A. S. Mériaux, M. Caffee, G. Zao, and Q. He (1998), Holocene left slip-rate determined by cosmogenic surface dating on the Xidatan segment of the Kunlun fault (Qinghai, China), *Geology*, *26*, 695–698.

Van der Woerd, J., P. Tapponnier, F. J. Ryerson, A. S. Mériaux, B. Meyer, Y. Gaudemer, R. C. Finkel, M. W. Caffee, G. G. Zhao, and Z. Q. Xu (2002), Uniform postglacial slip-rate along the central 600 km of the Kunlun Fault (Tibet), from Al-26, Be-10, and C-14 dating of riser offsets, and climatic origin of the regional morphology, *Geophys. J. Int.*, *148*, 356–388.

Van der Woerd, J., Y. Klinger, K. Sieh, P. Tapponnier, F. J. Ryerson, and A.-S. Mériaux (2006), Long-term slip rate of the southern San Andreas Fault from ^{10}Be–^{26}Al surface exposure dating of an offset alluvial fan, *J. Geophys. Res.*, *111*, B04407, doi:10.1029/2004JB003559.

Wdowinski, S., Y. Bock, G. Baer, L. Prawirodirdjo, N. Bechor, S. Naaman, R. Knafo, Y. Forrai, and Y. Melzer (2004), GPS measurements of current crustal movements along the Dead Sea Fault, *J. Geophys. Res.*, *109*, B05403, doi:10.1029/2003JB002640.

Weldon, R., T. Fumal, and G. Biasi (2004), Wrightwood and the earthquake cycle: What a long recurrence record tells us about how faults work, *GSA Today*, *14*(9), 4–10.

Wells, S. G., L. D. McFadden, J. Poths, and C. T. Olinger (1995), Cosmogenic ^{3}He surface-exposure dating of stone pavements: Implications for landscape evolution in deserts, *Geology*, *23*(7), 613–616.

Wright, T. J., B. Parsons, P. C. England, and E. J. Fielding (2004), InSAR observations of low slip rates on the major faults of western Tibet, *Science*, *305*, 236–239.

Zak, I., and R. Freund (1966), Recent strike slip movements along the Dead Sea Rift, *Isr. J. Earth Sci.*, *15*, 33–37.

M. Al-Qaryouti and O. Mayyas, Geology Department, American University of Beirut, Beirut, Lebanon.

A. Elias, Geology Department, American University of Beirut, Riad el Solh, Beirut 1107-2020, Lebanon.

R. C. Finkel, EPS Department, University of California Berkeley, Berkeley, CA 94720, USA.

Y. Klinger, Equipe de Tectonique, Institut de Physique du Globe de Paris, CNRS, 4 Place Jussieu, Box 89, F-75252 Paris Cedex 05, France. (lebeon@ipgp.jussieu.fr)

M. Le Béon, Department of Geosciences, National Taiwan University, 1 Roosevelt Rd. Sec. 4, 10617 Taipe, Taiwan.

A.-S. Mériaux, School of Geography, Politics and Sociology, Newcastle University, Newcastle upon Tyne NE1 7RU, UK.

F. J. Ryerson, Institute of Geophysics and Planetary Physics, Lawrence Livermore National Laboratory, Livermore, CA 94550, USA.

P. Tapponnier, Earth Observatory of Singapore, Nanyang Technological University, 50 Nanyang Ave., Block N2-01a-15, Singapore 639798.